

## RESEARCH ARTICLE

BICCN

# Comparative transcriptomics reveals human-specific cortical features

Nikolas L. Jorstad<sup>1†</sup>, Janet H. T. Song<sup>2,3,4,5†</sup>, David Exposito-Alonso<sup>2,3,4,5†</sup>, Hamsini Suresh<sup>6</sup>, Nathan Castro-Pacheco<sup>6</sup>, Fenna M. Krienen<sup>7</sup>, Anna Marie Yanny<sup>1</sup>, Jennie Close<sup>1</sup>, Emily Gelfand<sup>1</sup>, Brian Long<sup>1</sup>, Stephanie C. Seeman<sup>1</sup>, Kyle J. Travaglini<sup>1</sup>, Soumyadeep Basu<sup>8,9</sup>, Marc Beaudin<sup>2,3,4,5</sup>, Darren Bertagnolli<sup>1</sup>, Megan Crow<sup>6,10</sup>, Song-Lin Ding<sup>1</sup>, Jeroen Eggemont<sup>8</sup>, Alexandra Glandon<sup>1</sup>, Jeff Goldy<sup>1</sup>, Katelyn Kiick<sup>1</sup>, Thomas Kroes<sup>8</sup>, Delissa McMillen<sup>1</sup>, Trangthanh Pham<sup>1</sup>, Christine Rimorin<sup>1</sup>, Kimberly Siletti<sup>11</sup>, Saroja Somasundaram<sup>1</sup>, Michael Tieu<sup>1</sup>, Amy Torkelson<sup>1</sup>, Guoping Feng<sup>12,13,14</sup>, William D. Hopkins<sup>15</sup>, Thomas Hölt<sup>9</sup>, C. Dirk Keene<sup>16</sup>, Sten Linnarsson<sup>11</sup>, Steven A. McC Carroll<sup>7,17</sup>, Boudewijn P. Lelieveldt<sup>8,18</sup>, Chet C. Sherwood<sup>19</sup>, Kimberly Smith<sup>1</sup>, Christopher A. Walsh<sup>2,3,4,5</sup>, Alexander Dobin<sup>6</sup>, Jesse Gillis<sup>20</sup>, Ed S. Lein<sup>1</sup>, Rebecca D. Hodge<sup>1\*</sup>, Trygve E. Bakken<sup>1\*</sup>

The cognitive abilities of humans are distinctive among primates, but their molecular and cellular substrates are poorly understood. We used comparative single-nucleus transcriptomics to analyze samples of the middle temporal gyrus (MTG) from adult humans, chimpanzees, gorillas, rhesus macaques, and common marmosets to understand human-specific features of the neocortex. Human, chimpanzee, and gorilla MTG showed highly similar cell-type composition and laminar organization as well as a large shift in proportions of deep-layer intratemporal-projecting neurons compared with macaque and marmoset MTG. Microglia, astrocytes, and oligodendrocytes had more-divergent expression across species compared with neurons or oligodendrocyte precursor cells, and neuronal expression diverged more rapidly on the human lineage. Only a few hundred genes showed human-specific patterning, suggesting that relatively few cellular and molecular changes distinctively define adult human cortical structure.

**H**umans have distinctive cognitive abilities compared with nonhuman primates (NHPs), including chimpanzees, which are our closest evolutionary cousins. For example, humans have a capacity for vocal learning that requires a highly interconnected set of brain regions, including the middle temporal gyrus (MTG) region of the neocortex, which integrates multimodal sensory information and is critical for visual and auditory language comprehension (1, 2). Human MTG is larger and more connected to other language-associated cortical areas than the MTG of chimpanzees and other NHPs (3–5). These gross anatomical differences may be accompanied by changes in the molecular programs of cortical neurons and non-neuronal cells. Indeed, previous work has identified hundreds of genes with up- or down-regulated expression in the cortex of humans compared with that of chimpanzees and other primates (6–9) but have been limited to comparing broad populations of cells or have lacked another great ape species in which to study changes specific to the human lineage.

Single-nucleus RNA sequencing (snRNA-seq) has enabled the generation of high-resolution transcriptomic taxonomies of cell types in the neocortex and other brain regions. Comparative analysis has established homologous cell types across mammals, including humans and NHPs, and identified conserved and specialized

features: cellular proportions (10), spatial distributions (11), and transcriptomic and epigenomic profiles (12). In this study, we profiled more than 570,000 single nuclei using RNA sequencing from the MTG of five species: human, two other great apes (chimpanzee and gorilla), a cercopithecid monkey (rhesus macaque), and a platyrhine monkey (common marmoset). On the basis of a recently published mammalian phylogeny (13), this represents approximately 38 million years of evolution since these primate species shared a last common ancestor and encompasses the relatively recent divergence of the human lineage from that of chimpanzees at 6 million years ago.

We defined cell-type taxonomies for each species and a consensus taxonomy of 57 homologous cell types that were conserved across these primates. This enabled a comparison of the cellular architecture of the cortex in humans with that of a representative sample of non-human primates at high resolution to disentangle evolutionary changes in cellular composition from gene expression profiles. Including gorillas as a third great apes species enabled us to infer which differences between humans and chimpanzees are newly evolved in humans. Including two phylogenetically diverse monkey species enabled us to identify the cellular specializations that humans share with other great apes that may contribute to our enhanced cognitive abilities. Finally,

we identified a subset of changes that may be adaptive by establishing putative links between human accelerated regions (HARs) and human conserved deletions (hCONDELs) and human expression specializations by leveraging recently generated datasets of the in vitro activity of HARs (14) and cell type-specific chromatin folding (15, 16).

## Within-species cell-type taxonomies

MTG cortical samples were collected from postmortem adult male and female human, chimpanzee (*Pan troglodytes*), gorilla (*Gorilla gorilla*), rhesus macaque (*Macaca mulatta*), and common marmoset (*Callithrix jacchus*) individuals for snRNA-seq (Fig. 1B). MTG was identified in each species using gross anatomical landmarks. Layer dissections for human, chimpanzee, and gorilla datasets were identified and sampled as previously described (17). MTG slabs were sectioned and stained with fluorescent Nissl, and layers were microdissected and processed separately for nuclear isolation.

For humans, single nuclei from seven individuals contributed to three RNA-seq datasets: a Chromium 10x v3 (Cv3) dataset sampled from all six cortical layers ( $n = 107,000$  nuclei), a Cv3 dataset sampled from microdissected layer 5 to capture rare excitatory neuron types ( $n = 36,000$ ), and our previously characterized (17) SMARTseq v4 (SSv4) dataset of six microdissected layers ( $n = 14,500$ ). Chimpanzee

<sup>1</sup>Allen Institute for Brain Science, Seattle, WA 98109, USA.

<sup>2</sup>Allen Discovery Center for Human Brain Evolution, Boston Children's Hospital and Harvard Medical School, Boston, MA 02115, USA. <sup>3</sup>Division of Genetics and Genomics, Boston Children's Hospital, Boston, MA 02115, USA. <sup>4</sup>Department of Pediatrics and Neurology, Harvard Medical School, Boston, MA 02115, USA. <sup>5</sup>Howard Hughes Medical Institute, Boston Children's Hospital, Boston, MA 02115, USA. <sup>6</sup>Cold Spring Harbor Laboratory, Cold Spring Harbor, NY 11724, USA.

<sup>7</sup>Department of Genetics, Harvard Medical School, Boston, MA 02115, USA. <sup>8</sup>LKEB, Department of Radiology, Leiden University Medical Center, Leiden, Netherlands. <sup>9</sup>Computer Graphics and Visualization Group, Delft University of Technology, Delft, Netherlands. <sup>10</sup>Stanley Institute for Cognitive Genomics, Cold Spring Harbor Laboratory, Cold Spring Harbor, NY 11724, USA. <sup>11</sup>Department of Medical Biochemistry and Biophysics, Karolinska Institutet, Stockholm, Sweden. <sup>12</sup>McGovern Institute for Brain Research, Massachusetts Institute of Technology, Cambridge, MA 02139, USA. <sup>13</sup>Department of Brain and Cognitive Sciences, Massachusetts Institute of Technology, Cambridge, MA 02139, USA. <sup>14</sup>Stanley Center for Psychiatric Research, Broad Institute of MIT and Harvard, Cambridge, MA 02142, USA. <sup>15</sup>Keeling Center for Comparative Medicine and Research, University of Texas, MD Anderson Cancer Center, Houston, TX 78602, USA. <sup>16</sup>Department of Laboratory Medicine and Pathology, University of Washington, Seattle, WA 98195, USA. <sup>17</sup>Broad Institute of MIT and Harvard, Cambridge, MA 02142, USA. <sup>18</sup>Pattern Recognition and Bioinformatics Group, Delft University of Technology, Delft, Netherlands. <sup>19</sup>Department of Anthropology, The George Washington University, Washington, DC 20037, USA.

<sup>20</sup>Department of Physiology, University of Toronto, Toronto, ON, Canada.

\*Corresponding author. Email: trygveb@alleninstitute.org (T.E.B.); rebeccah@alleninstitute.org (R.D.H.)  
†These authors contributed equally to this work.

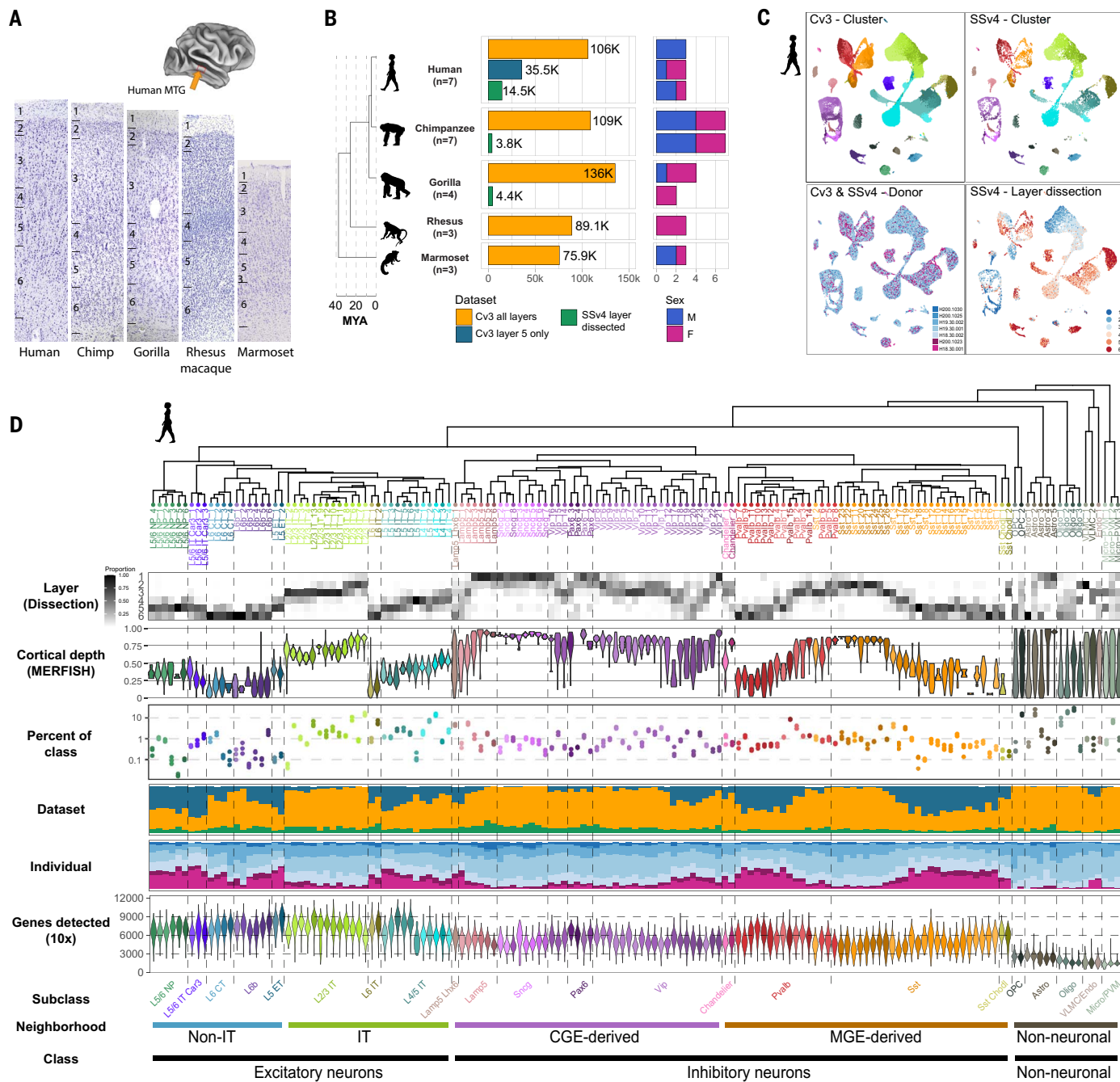


**Fig. 1. Transcriptomic cell-type taxonomies of human and NHP MTG.**

(A) Representative Nissl-stained cross sections of MTG in the five species profiled. The inset shows the approximate MTG region dissected from human brain. (B) Phylogeny of species (left; MYA, millions of years ago) and bar plots of nuclei that passed quality control (center) and sampled individuals (right) for each dataset. (C) Uniform manifold approximation and projection (UMAP) plots of single nuclei from human MTG integrated across individuals and RNA-seq technologies and colored by cluster, individual ID, and dissected layer. (D) From top to bottom are the following: a human taxonomy dendrogram based on Cv3 cluster median expression; a heatmap of laminar distributions estimated from

SSV4 layer dissections; violin plots of the relative cortical depth (pia to white matter) of cells grouped by type based on in situ measurement of marker expression in human MTG; a dot plot of cell-type abundance represented as a proportion of class (excitatory, inhibitory, glia), where error bars denote standard deviation across Cv3 individuals (L5 is the only dissection excluded); bar plots indicating the proportion of each cluster that is composed of Cv3 all layers, Cv3 layer 5 only, and SSV4 layer dissected datasets; bar plots indicating the proportion of each cluster that is composed of each individual; and violin plots showing the number of distinct genes detected from Cv3 datasets.

( $n = 7$  individuals) datasets included Cv3 across layers ( $n = 109,000$  nuclei) and SSV4 layer dissections ( $n = 3900$ ), and gorilla ( $n = 4$ ) datasets included Cv3 ( $n = 136,000$ ) and SSV4

( $n = 4400$ ). Macaque ( $n = 3$ ) and marmoset ( $n = 3$ ) datasets included Cv3 from all layers ( $n = 89,700$  and 76,900 nuclei, respectively). All nuclei preparations were stained for the pan-neuronal

marker NeuN and purified by fluorescence-activated cell sorting (FACS) to enrich for neurons over non-neuronal cells. Samples containing 90% NeuN<sup>+</sup> (neurons) and 10% NeuN<sup>-</sup>

(non-neuronal cells) nuclei were used for library preparations and sequencing. Nuclei from Cv3 experiments were sequenced to a saturation target of 60%, resulting in approximately 120,000 reads per nucleus. Nuclei from SSv4 experiments were sequenced to a target of 500,000 reads per nucleus.

Each species was independently analyzed to generate a “within-species” taxonomy of cell types. First, datasets were annotated with cell subclass labels from our published human MTG and primary motor (M1) taxonomies (12, 17) using Seurat (18). Cell types were grouped into five neighborhoods—intratelencephalic (IT)—projecting and non-IT-projecting excitatory neurons, caudal ganglionic eminence (CGE)—and medial ganglionic eminence (MGE)—derived interneurons, and non-neuronal cells—that were analyzed separately. High-quality nuclei were normalized using SCTransform (19) and integrated across individuals and data modalities using canonical correlation analysis. Human nuclei were well mixed across the three datasets and across individuals (Fig. 1C), and similar mixing was observed for the other species (figs. S1 and S2). The integrated space was clustered into small “metacells” that were merged into 151 clusters (Fig. 1D and fig. S3) that included nuclei from all datasets and individuals. Cell types had robust gene detection (neuronal, median 3000 to 9000 genes; non-neuronal, median 1500 to 3000 genes) and were often rare (less than 1 to 2% of the cell class) and restricted to one or two layers (table S1). Single nuclei from the other four species were clustered using identical parameters, resulting in 109 clusters in chimpanzees (fig. S1A), 116 in gorillas (fig. S1B), 120 in macaques (fig. S2A), and 104 in marmosets (fig. S2B). Humans had the most cell-type diversity (151 clusters), although the number of cell types could have been driven by technical factors: sampled individuals (only female macaques), tissue dissections (additional layer 5 sampling for humans), RNA-seq method (SSv4 included for great apes), and genome annotation quality.

Species cell types were hierarchically organized into dendograms based on transcriptomic similarity (Fig. 1D and figs. S1 to S3) and grouped into three major cell classes: excitatory (glutamatergic) neurons, inhibitory [ $\gamma$ -aminobutyric acid-releasing (GABAergic)] neurons, and non-neuronal cells. Each of the three major classes were further divided into cell neighborhoods and subclasses based on an integrated analysis of marker gene expression, layer dissections, and comparison with published cortical cell types (12). In total, we identified 24 conserved subclasses (18 neuronal, 6 non-neuronal) (fig. S4A) that were used as a prefix for cell-type labels. Inhibitory neurons comprised five CGE-derived subclasses (*LAMP5*, *LHX6*, *LAMP5*, *VIP*, *PAX6*, and *SNCG*) expressing the marker *ADARB2* and four MGE-derived sub-

classes (Chandelier, *PVALB*, *SST*, and *SST CHDL*) expressing *LHX6*. Excitatory neurons include five IT-projecting subclasses (L2/3 IT, L4 IT, L5 IT, L6 IT, and L5/6 IT *CAR3*) and four deep-layer non-IT-projecting subclasses (L5 ET, L5/6 NP, L6b, and L6 CT). Non-neuronal cells were grouped into six subclasses: astrocytes, oligodendrocyte precursor cells (OPCs), oligodendrocytes, microglia and perivascular macrophages (micro/PVMs), endothelial cells, and vascular and leptomeningeal cells (VLMCs).

This human MTG taxonomy provided substantially higher cell-type resolution than our previously published human cortical taxonomies (12, 17), likely because of increased sampling (155,000 versus 15,000 to 85,000 nuclei; fig. S3). Furthermore, the *in situ* spatial distributions of cell types were characterized using MERFISH and are included as a gallery of human MTG sections (data S1) and summarized by cortical depth (Fig. 1D). All cell types matched one to one or one to many, and diversity was particularly expanded for non-neuronal subclasses and several neuronal subclasses and types: L5/6 NP (six types), L6 CT (four types), L2/3 IT *FREM3* (eight types), and *SST CALB1* (nine types). The *FREM3* subtypes had a graded distribution across layers 2 and 3, consistent with spatial variation in *FREM3* neuron morphology and electrophysiology (20).

#### Divergent abundances of cell types

Neuronal subclass frequencies were estimated as a proportion of excitatory and inhibitory neuron classes based on snRNA-seq sampling to account for species differences in the ratio of excitatory to inhibitory neurons (E:I ratio) (fig. S4B) (12). Subclass proportions were highly consistent across individuals within each species and varied significantly [one-way analysis of variance (ANOVA),  $P < 0.05$ ] across species (Fig. 2A). Post hoc pairwise *t* tests between humans and each NHP identified up to fivefold more L5/6 IT *CAR3*, L5 ET, and *PVALB*-expressing chandelier interneurons in marmosets. Interestingly, L2/3 IT neurons had similar proportions in the MTG, in contrast to the 50% expansion of L2/3 IT neurons in humans versus marmosets in M1 (12).

Among L5/6 IT *CAR3* neurons, two distinct subtypes had high and low *CUX2* expression, respectively, in all species (Fig. 2B). *HTR2C* and *MGAT4C* were additional conserved markers of the high-*CUX2* subtype, and *BCL11A* and *LDB2* were markers of the low-*CUX2* subtype (Fig. 2C). Subtype proportions were balanced in great apes, mostly low-*CUX2* in macaques, and mostly high-*CUX2* in marmosets (Fig. 2D). Low-*CUX2* neurons were consistently more enriched in deeper layers than high-*CUX2* neurons in all three great apes (Fig. 2E). In human and macaque MTG, *in situ* labeling of marker genes using MERFISH (Fig. 2F) validated that the low-*CUX2* subtype was enriched at the

border of layers 5 and 6, and the high-*CUX2* subtype extended from upper layer 6 through layer 5. In macaque MTG, the proportion of high-*CUX2* neurons varied along the gyrus (Fig. 2F) with little on the ventral side, consistent with the snRNA-seq data, and more on the dorsal side. In marmosets, *in situ* labeling of marker genes using RNAscope showed that high-*CUX2* neurons were enriched in MTG (TPO and TE3), consistent with snRNA-seq data, and in adjacent secondary auditory regions (Fig. 2F). On the basis of the snRNA-seq data that we collected from seven additional regions of the human cortex (21), low-*CUX2* neurons were more common in many regions, and high-*CUX2* neurons were enriched in temporal cortex (MTG and primary auditory, A1) and parietal cortex (angular gyrus, ANG and primary somatosensory, S1) (Fig. 2G). Similarly, snRNA-seq data collected from six additional regions of the marmoset cortex (10, 12, 22) revealed that the high-*CUX2* subtype was most enriched in temporal areas (MTG and A1) and less enriched in S1 (Fig. 2G).

#### Primate specializations of cell-type expression

Next, we compared the transcriptomic similarity of subclasses across primates. For each species, we defined gene markers that could reliably predict the subclass identities of cells and were filtered to include one-to-one orthologs (table S2). Non-neuronal subclasses expressed hundreds of markers and demonstrated greater distinction than neuronal subclasses that had 50 to 100 markers. Each subclass had a similar number of markers in all species (Fig. 3A), but only 10 to 20% had strongly conserved specificity (Fig. 3, A and B). To compare the global expression profile of subclasses across primates, we correlated normalized median expression of variable genes between each species pair for each cell subclass (excluding undersampled endothelial cells and VLMCs) (Fig. 3C). Glial cells (except OPCs) had greater expression changes between species compared with neurons. Expression similarity decreased with evolutionary distance between human and NHPs at a similar rate across neuronal subclasses and OPCs and faster in oligodendrocytes, astrocytes, and microglia in particular (Fig. 3D). Glial expression remained more divergent across species after normalizing for increased variation within species (fig. S4C). Chimpanzee neuronal subclasses were more similar to those of gorillas than to those of humans (Fig. 3E), despite a more recent common ancestor with humans (6 million versus 7 million years ago). This was consistent with the faster evolution of neurons on the human lineage since the divergence with chimpanzees. By contrast, there was no evidence for faster divergence among non-neuronal cells on the human lineage (Fig. 3E) or on the lineage leading to great apes (fig. S4D).

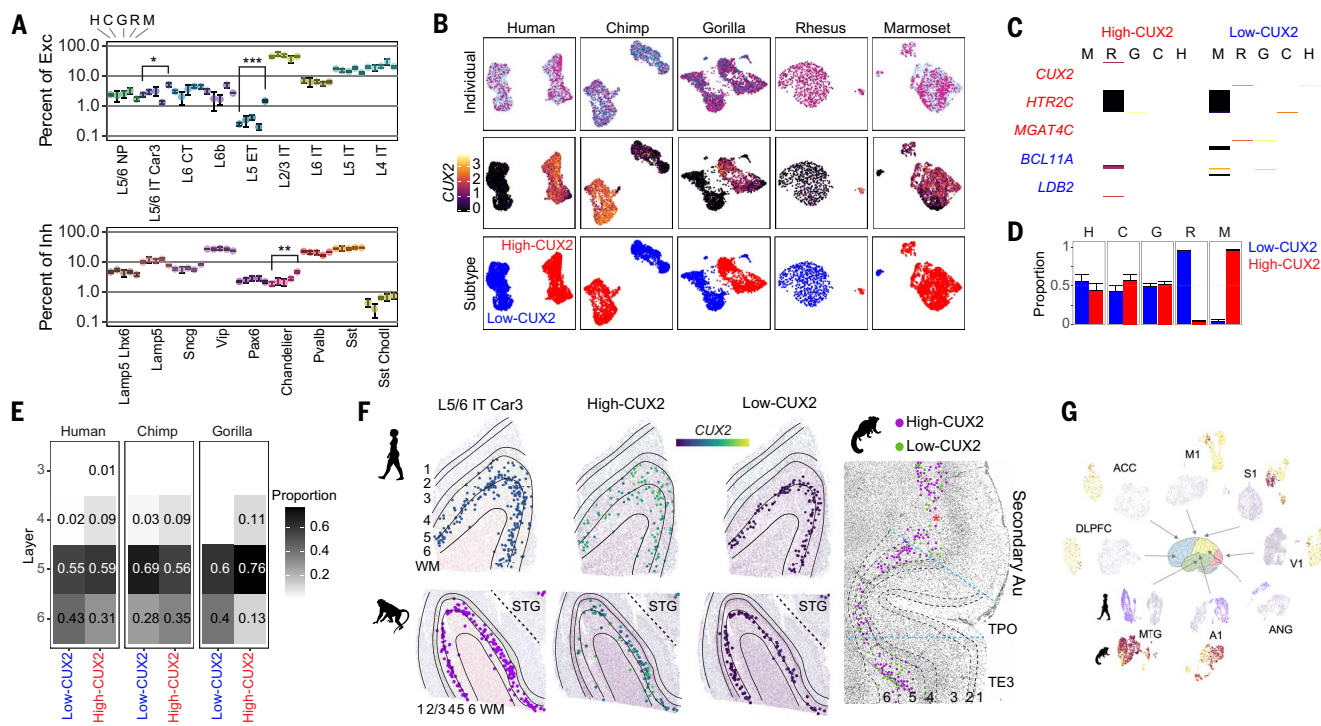


**Fig. 2. Great ape specialization of L5/6 IT CAR3 neuron proportions.**

(A) Average subclass proportions of neuronal classes (error bars indicate standard deviation across individuals). Significant differences in proportions as compared to human are shown (two-sided *t* tests; Benjamini-Hochberg-corrected \* $P < 0.05$ , \*\* $P < 0.01$ , and \*\*\* $P < 0.001$ ). Exc., excitatory; Inh., inhibitory. (B) UMAPs of L5/6 IT CAR3 neurons labeled by individual, CUX2 expression, and subtype. (C) Conserved marker gene expression of high-CUX2 and low-CUX2 subtypes. (D) Average proportions of L5/6 IT CAR3 neuron subtypes (error bars indicate standard deviation across individuals). (E) Laminar distributions of subtypes across great apes estimated on the

basis of layer dissections. (F) L5/6 IT CAR3 neurons labeled in situ on the basis of marker expression in human and macaque MTG and in the matching regions in marmoset cortex (TPO and TE3). Low-CUX2 neurons are enriched at the L5/6 border in human and macaque. The red asterisk indicates the area of low probe density due to a technical artifact. Au, auditory cortex; STG, superior temporal gyrus; WM, white matter. (G) UMAPs of CUX2 expression in L5/6 IT CAR3 neurons from matched cortical regions in humans (purple, high expression) and marmosets (dark orange, high expression). H, human; C, chimpanzee; G, gorilla; R, rhesus macaque; M, marmoset.

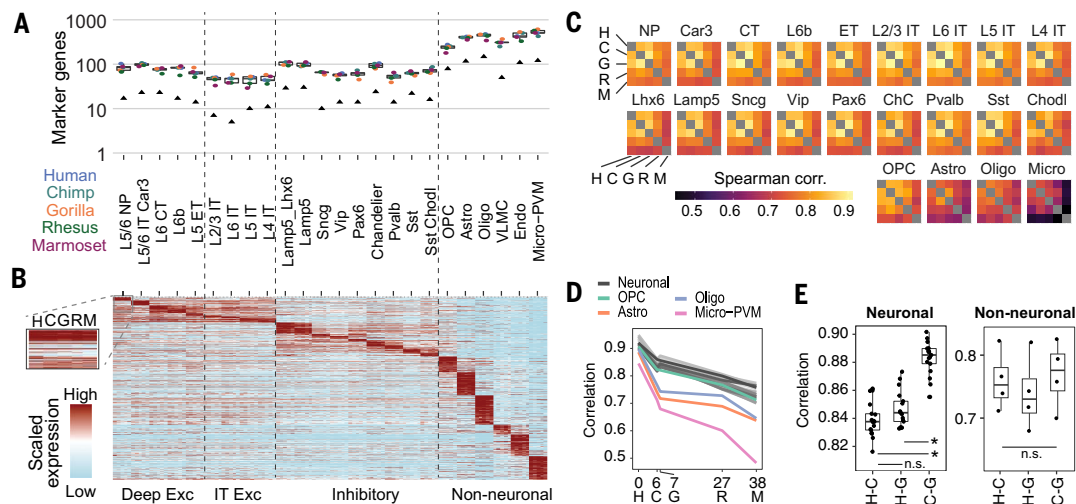


**Fig. 3. Rapid divergence of neuronal expression on the human lineage.**

(A) Box plot showing the distribution of subclass marker genes across species. Points denote the number of species markers, and black triangles denote the number of conserved markers. (B) Expression heatmap for 924 conserved markers shown in (A). Expression is row-scaled for each subclass for each species. (C) Heatmaps showing Spearman correlations of subclass median expression for all variable genes between species. (D) Line graph of subclass correlations from (C) for humans compared to each NHP as a function of the

evolutionary distance (millions of years ago) of the most recent common ancestor (13). The zero point denotes the median correlation between human individuals for each subclass. (E) Box plots of great ape pairwise correlations for neuronal (left) and non-neuronal (right) subclasses from (C). ANOVA and post hoc two-sided *t* tests; Benjamini-Hochberg-corrected \* $P < 0.05$ . Non-neuronal ANOVA was not significant (n.s.). For box plots in (A) and (E), the center line represents the median, box limits are upper and lower quartiles, and whiskers are minimum and maximum values.

In addition to evolutionary changes in gene transcript amounts, there may be changes in transcript isoform usage. We quantified isoform expression using full-length transcript information from SSv4 RNA-seq data acquired from great apes. For each cell subclass, we identified differentially expressed genes (DEGs) (table S3) and genes with at least moderately high expression that strongly switched isoform usage between each pair of species (table S4). There was little overlap between genes with differential expression and isoform usage for L2/3 IT neurons (fig. S4E). Genes with a human-specialized switch in isoform expression included *BCARI*, *INO80B*, and *SBNO1* (fig. S4F). *BCARI* is a scaffold protein that is a component of the netrin signaling pathway and is involved in axon guidance (23). *INO80B* (24) and *SBNO1* are involved in chromatin remodeling, and *SBNO1* contributes to brain-axis development in zebrafish (25) and is a risk gene for intellectual disability (26). The predominant isoform of *INO80B* in human L2/3 IT neurons includes a retained intron (fig. S4G) that may suppress transcription of this gene (27) and contribute to human specializations.

Finally, we quantified the conservation of gene expression patterns across cell types

between humans and NHPs. As expected, expression differences increased with evolutionary distance (fig. S4H), and 75% of genes were conserved in all species [Spearman correlation ( $r$ ) > 0.9 in great apes;  $r$  > 0.65 in marmosets]. Highly divergent expression ( $r$  < 0.25) was observed for 651 genes and often in only a single species (fig. S4I), such as *FAM177B*, which was exclusively expressed in human microglia (fig. S4J). A few genes had fixed derived expression in the great ape lineage. For instance, *MEPE* encodes a secreted calcium-binding phosphoprotein, and its expression was restricted to *PVALB*-expressing interneurons in great apes (fig. S4J); prolactin receptor (*PRLR*) had enriched expression in *SST*-expressing interneurons and L5/6 IT *CAR3* neurons in great apes compared with CGE-derived interneurons in macaques and marmosets, which potentially alters hormonal modulation of these neurons.

### Human specializations of glial cells

Because glial cells exhibited the most divergent gene expression changes across species (Fig. 3, C and D), we next aimed to uncover their specialized transcriptional programs in humans versus other great apes. For astrocytes, we found more human DEGs (1189)

than chimpanzee (787) or gorilla (617) DEGs (Fig. 4, A and B; fig. S5A; and table S3) and three times more highly divergent (>10-fold) human DEGs (Fig. 4A). Human astrocyte DEGs were enriched in synaptic signaling and protein translation pathways on the basis of enrichment analyses using Gene Ontology (GO) (Fig. 4C) and Synaptic GO (SynGO) (28) (Fig. 4D and fig. S5B) databases. To study synapse-related astrocytic gene programs, we used a molecular database of astrocyte cell-surface molecules enriched at astrocyte-neuron junctions from an in vivo proteomic labeling approach in the mouse cortex (29). Among genes encoding 118 proteins that were robustly enriched in perisynaptic astrocytic processes, 24 genes (20%) were differentially expressed in human astrocytes compared with chimpanzee and gorilla astrocytes (Fig. 4E), and 47 genes (40%) had conserved expression across great apes (fig. S5, C and D). Neuroligins and neurexins, which are ligand-receptor pairs that play a key role in astrocytic morphology and synaptic development (30), showed divergent expression patterns across great ape species (Fig. 4, F and G). Other cell-adhesion gene families with well-known functions in astrocytic morphological and synaptic development also had multiple

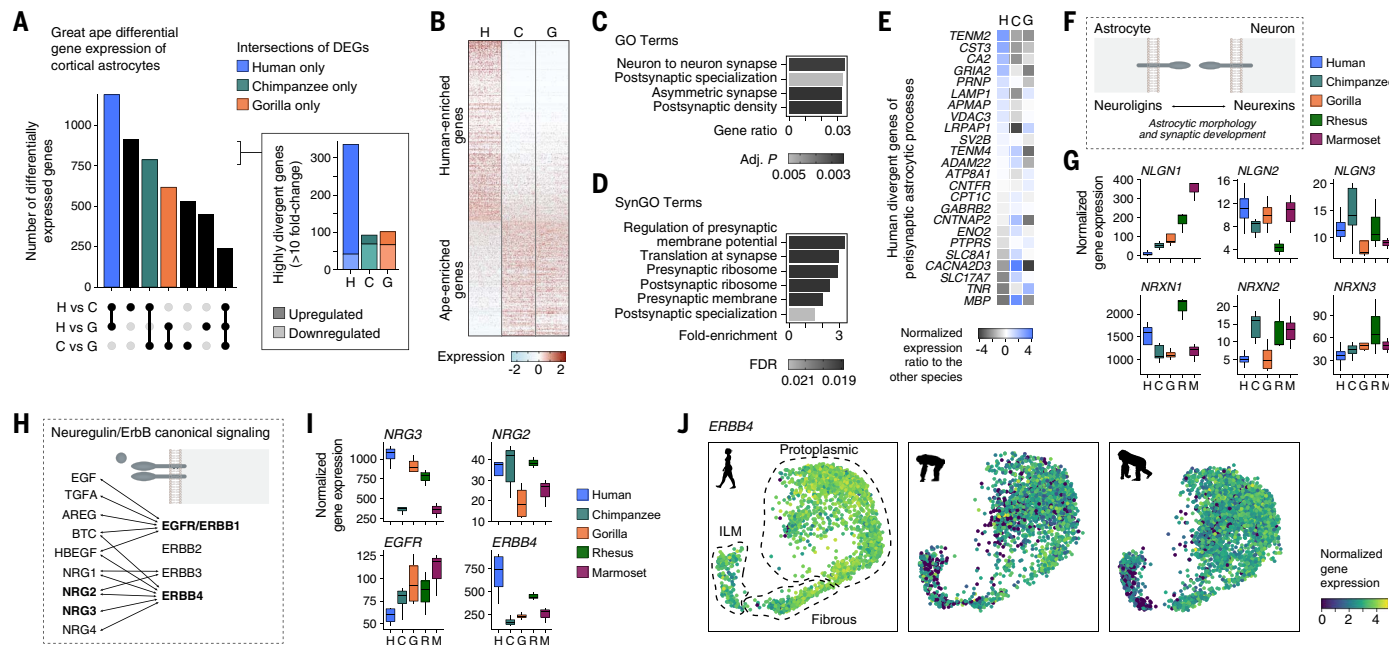


**Fig. 4. Human cortical astrocytes have specialized molecular features.**

(A) Upset plot showing the number of DEGs in cortical astrocytes for pairwise comparisons between great ape species. The inset shows the number of highly divergent genes (fold change >10). (B) Heatmap showing row-scaled expression of human DEGs versus chimpanzee and gorilla DEGs. (C and D) Significantly enriched GO (C) and SynGO (D) terms in the union of astrocyte DEGs from the pairwise comparison between human and chimpanzee and the pairwise comparison between human and gorilla (FDR <0.05). (E) Heatmap showing human DEGs (FDR <0.01, normalized gene count >5) of the proteome of perisynaptic astrocytic processes (29). (F) Schematic illustrating the trans-cellular interaction of astrocytic neuroligins and neuronal neurexins that is known

to play a role in astrocytic morphology and synaptic development. (G) Box plots showing differential gene expression of neuroligins and neurexins in astrocytes across primate species. (H) Schematic illustrating ligand-receptor interactions of the neuregulin-ErbB signaling pathway. (I) Box plots showing differential expression of the ligand-encoding genes *NRG2* and *NRG3* and the receptor-encoding genes *EGFR* and *ERBB4* in astrocytes across primate species. (J) Gene expression patterns of *ERBB4* across astrocyte subtypes and great ape species. The dashed lines indicate the labeled astrocyte subtypes. ILM, interlaminar. For box plots in (G) and (I), the center line represents the median, box limits are upper and lower quartiles, and whiskers are minimum and maximum values.

members among human astrocyte DEGs, including ephrins and their cognate receptors (*EFNA5*, *EPHA6*), clustered protocadherins (*PCDH9*), and teneurins (*TENM2*, *TENM3*, *TENM4*) (fig. S5, D and F).

In addition to cell-adhesion programs, we explored other cell-surface or secreted ligands and receptors that contribute to astrocyte function. We found that several astrocyte-secreted synaptogenic molecules, such as osteonectin (*SPARC*) and hevin (*SPARCL1*), and extracellular matrix (ECM)-related proteins (brevican, *BCAN*; neurocan, *NCAN*; and phosphacan, *PTPRZ1*) were up-regulated in human astrocytes (fig. S5, E and F). Of note, four members of the neuregulin-ErbB signaling pathway showed differential gene expression in great ape astrocytes, with two receptors (*EGFR* and *ERBB4*) displaying expression changes in opposite directions (Fig. 5, I and J). Up-regulation of human *ERBB4* expression was higher in protoplasmic and fibrous astrocytes than in interlaminar astrocytes (Fig. 3J and fig. S5G), demonstrating that transcriptional specializations can occur in a subtype-specific fashion. Finally, glutamate AMPA receptor subunits (*GRIA1*, *GRIA2*, *GRIA4*) had more than threefold greater expression in human astrocytes compared with chimpanzee and gorilla astrocytes, suggesting a human-

specific astrocyte responsiveness to glutamate (fig. S5H).

We next examined gene expression changes in microglia, which also play critical roles in cortical circuit formation (31, 32). Recent comparative spatial transcriptomic data indicate that microglia-neuron contacts are more prevalent in human cortical circuits compared with those of mice, particularly in superficial layers (33). We reasoned that evolutionary changes in microglial connectivity could be mediated by fine-tuning the expression of cell-surface ligands and receptors. Indeed, we found that human microglia have more DEGs (328) than chimpanzee (175) or gorilla (164) microglia (fig. S6, A to C), and human DEGs were overrepresented in GO and SynGO terms related to synaptic compartments (fig. S6, D to F). Among the human microglia DEGs were several disease-associated genes, including *SNCA* (which encodes  $\alpha$ -synuclein) and *TMEM163*, which are implicated in neurodegenerative disorders (34–36), and Kalirin (*KALRN*), which is associated with neurodevelopmental and neuropsychiatric disorders (37) (fig. S6G). We also corroborated the human-specific up-regulation of *FOXP2* and *CACNA1D*, of which the latter was recently reported in the dorsolateral prefrontal cortex (9).

Oligodendrocytes also showed human specializations, including DEGs involved in myelin organization and cell adhesion (for example, *CNTNAP2* and *LAMA2*) (fig. S6). Unlike astrocytes and microglia, human and chimpanzee oligodendrocytes had similar numbers of DEGs, although humans had more up-regulated, highly divergent DEGs (fig. S6I). These findings support faster divergence of glial expression in the human lineage that parallels neuronal divergence and likely affects interactions between glia and neurons.

### Consensus cell-type conservation and divergence

To further investigate the canonical architecture of primate MTG, we built a transcriptomic taxonomy of high-resolution consensus cell types. Starting with CGE-derived interneurons, we integrated single-nucleus expression profiles across the five species based on conserved co-expression using Seurat (18). Within-species cell types remained distinct, and nuclei were well integrated (Fig. 5, A and B, and fig. S7), particularly for humans and chimpanzees (fig. S12A). Similar results were observed for the other cell neighborhoods (figs. S8 to S11). Separate pairwise alignments between humans and NHPs confirmed that cell-type homologies were better resolved in more closely related

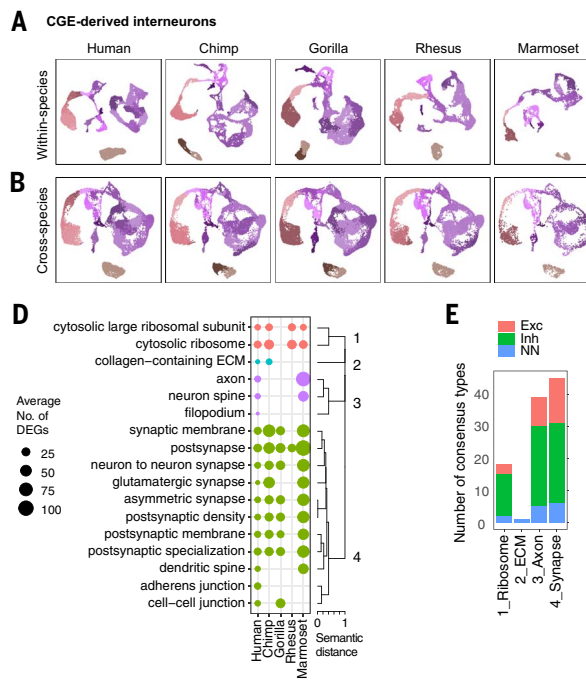
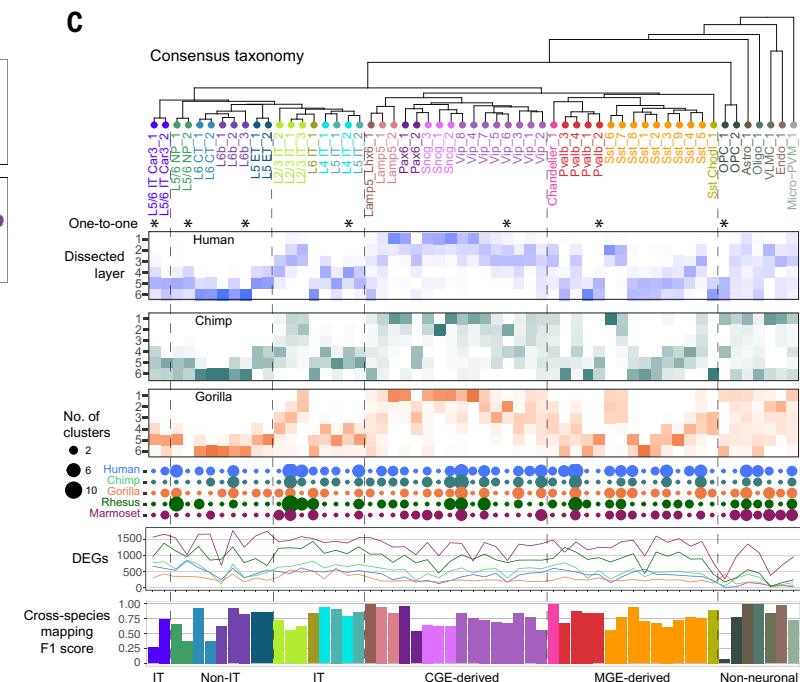


**Fig. 5. Divergent expression across conserved cell types.** (A) UMAPs of CGE-derived interneuron expression generated for each species and colored by within-species cell types. (B) UMAPs of CGE interneuron expression integrated across the five species and with the same coloring as (A). (C) Consensus taxonomy of 57 homologous cell types identified in all five species (asterisks indicate a one-to-one match across all species). For great ape species, heatmaps show the proportion of nuclei dissected from layers 1 through 6 for each type. The dot plot shows the number of within-species clusters that are associated with



each consensus type. The line plot shows the number of hDEGs per consensus type with with fold change >1.4 for each species (colors as in dot plot). The bar plot shows the average classification accuracy (F1 score) across the five species using scPolis (84) (fig. S12). (D) Summary of GO enrichment analysis of species DEGs. Cellular component terms that were significantly enriched for hDEGs in at least one consensus type and that form four distinct groups of similar GO terms are shown. (E) Summary of the number of consensus types that express hDEGs that were enriched for at least one term in the four semantic GO groups.

species (fig. S12B). We also found that excitatory neurons were less well integrated than inhibitory neurons, and this finding was consistent with greater species specializations of excitatory types.

We established homologous cell types between all pairs of species using MetaNeighbor, a statistical framework (38, 39) that identifies cell types that can be reliably discriminated [area under the receiver operating characteristic curve (AUROC)  $>0.6$ ] from nearest neighbors in one species based on training data from the other species or that are reciprocal best matches. Pairwise cell-type homologies were integrated to define 57 consensus types that included cell types that were identified in the five species, and a dendrogram was constructed based on transcriptomic similarities (Fig. 5C). The robustness of the 57 homologous types across species was confirmed using a complementary approach to consensus clustering, scArches (40) (fig. S12, C to H). Classification accuracy varied across consensus types (Fig. 5C) and with nearly perfect classification performance across species (average F1 score  $>0.95$ ) for distinct interneuron types (*LAMP5*, *LHX6*, *PAX6\_1*, and Chandelier cells) and non-neuronal types (astrocytes, oligodendrocytes, and endothelial cells). The rare *OPC\_1* subtype (5% of OPCs) had the lowest classification accuracy and somewhat ambiguous homology across species (fig. S11) and may represent different subpopulations of OPCs across species. Eight consensus types represented one-to-one matches across all species, and most of the types represented multiple matches of between 2 and 10 within-species types. Differential sampling of nuclei across species owing to differences in dissections or cell-type proportions might have contributed to the number of cell types that mapped to a consensus type. For example, in human MTG, more nuclei were sampled from layer 5 and more subtypes of the layer 5-enriched *SST\_3* consensus type were identified. Thus, there was a conserved set of cell types in primate MTG with transcriptomic specializations of subtypes. Laminar distributions of types were notably conserved across the great apes, except for *SST CHODL\_1*, which was present in more superficial layers of gorilla MTG (Fig. 5C), although more sampling of this rare type is needed for validation.

Previous work reported the lack of transcript and protein expression of tyrosine hydroxylase (*TH*), which encodes a key enzyme in the dopamine synthesis pathway, in the neocortex of non-human African great apes, including chimpanzees and gorillas (41, 42). Recent transcriptomic profiling of chimpanzee prefrontal cortex suggests that this represents a loss of dopamine signaling in a conserved cell type rather than a loss of a homologous type (9). In MTG, we identified nine consensus *SST*-expressing interneuron types present in all five

primates (Fig. 5E) that had robust sets of conserved and species-specific markers (fig. S13A and table S5). The *SST\_1* consensus type was distinct from most other MGE-derived interneurons (fig. S13B) and expressed *TH* in human, macaque, and marmoset neurons but not in chimpanzee or gorilla neurons (fig. S13, C to E). Conserved (for example, *NCAM2*, *PTPRK*, *UNC5D*, and *CNTNAP5*) and species-specific genes were enriched in pathways for connectivity and signaling (fig. S13, F to J). *SST\_1* was the rarest type in all primates (fig. S13K) and varied from 0.3% of *SST*-expressing interneurons in gorillas and macaques to 1 to 3% in humans, chimpanzees, and marmosets. Interestingly, most *TH*-expressing neurons belonged to different interneuron subclasses in humans (*SST*), macaques (*PVALB*), and marmosets (*VIP*) (fig. S13L), and this was confirmed by *in situ* labeling of *TH*-expressing neurons in human and macaque MTG (fig. S13M). Dopamine receptor expression varied across primates but did not track with predicted differences in local dopamine production (fig. S13, N and O). This is likely because subcortical regions provide most of the dopaminergic input to the neocortex and mask the effects of evolutionary changes in local input.

We tested for changes in the proportions of neuronal consensus types across primates using a Bayesian model (scCODA) that accounted for the compositional nature of the data (fig. S14A) (43). We found that the higher E:I ratio in marmosets (fig. S4B) was driven by increased proportions of most excitatory types, and the lower E:I ratio in macaques was driven by increased proportions of, in particular, *SST* and *VIP* interneuron types and by decreased proportions of *L2/3 IT\_2*, *L2/3 IT\_3*, and *L5/6 IT CAR3\_2* excitatory types. There were smaller changes among the great apes, except for an increased proportion of *L5/6 NP\_2* neurons in humans and chimpanzees.

Next, we identified species-specific genes by comparing consensus cell-type expression for each species to all other primates. Human consensus types had a broad range (fewer than 100 to more than 1000) of statistically significant DEGs (Fig. 5C and table S7) that represented 1 to 8% of expressed genes (fig. S14B). Excitatory types in deep layers (IT and non-IT) had the most human-specific DEGs (hDEGs), including *L5/6 NP\_2*, *L6 CT\_1*, and both subtypes of *L5/6 IT CAR3* neurons (Fig. 5C). Non-neuronal types had the fewest hDEGs despite having the lowest correlated expression between species (Fig. 2, D and E). Two factors contributed to this apparent inconsistency. First, non-neuronal cells expressed fewer transcripts than neurons, and the number of hDEGs as a proportion of median expressed genes was similar for non-neuronal and some neuronal types (fig. S14B). Second, non-neuronal cells were more variable across individuals than neurons (fig. S4C),

and there was reduced power to detect smaller expression changes. Indeed, non-neuronal and neuronal types with fewer hDEGs had larger median fold changes that were statistically significant despite high interindividual variation (fig. S14B).

Many species-specific DEGs were restricted to one or a few cell types, particularly for great apes (fig. S14C). The cell-type specificity of DEGs was not simply a result of expression changes in marker genes; it was also the result of selective changes in broadly expressed genes (fig. S14D). hDEGs had a median fourfold change in expression, whereas a few metabolism-related genes changed expression by 20-fold or more in most cell types (fig. S14E). The same genes were often differentially expressed in multiple species (fig. S14F) but in different cell types, and highly divergent ( $>10$ -fold) genes were usually found across all species. *In situ* measurement of two hDEGs, *COL1A1* and *DACH1*, validated enriched expression in human Chandelier and *L5/6 IT CAR3* neurons, respectively (fig. S14G). Species-specific DEGs were enriched in four major pathways: ribosomal processing, ECM, axon structure, and the synapse (Fig. 5, D and E). Ribosomal processing was primarily associated with interneurons in humans and all cell types in chimpanzees, macaques, and marmosets. ECM-associated DEGs, including several laminin genes, were specific to the *VLMC\_1* consensus type in humans, chimpanzees, and marmosets (fig. S14H) and have the potential to alter the blood brain barrier, as shown in a mouse model of pericyte dysfunction (44). Hundreds of axonal and synaptic genes were differentially expressed in most cell types in all species, and this suggests extensive molecular remodeling of connectivity and signaling during primate evolution.

### Enrichment of HARs and hCONDELs near human DEGs

Genes may change expression between species because of neutral or adaptive evolution. To investigate which hDEGs may be under positive selection, we linked hDEGs to human-specific genomic sequence changes. Because hDEGs are differentially expressed in only one or a few consensus cell types, expression changes are likely caused by sequence modifications to regulatory regions that can alter transcription in select cell types. We examined three previously identified classes of genomic regions that have changed along the human lineage: (i) HARs that are highly conserved across mammals and have higher substitution rates in the human lineage (45), (ii) hCONDELs that are highly conserved across mammals and deleted in humans (46, 47), and (iii) human ancestor quickly evolved regions (HAQERs) that are the fastest evolved regions in the human genome (47). We found that HARs and hCONDELs are

significantly [false discovery rate (FDR) <0.05] enriched near hDEGs in many consensus cell types (Fig. 6A and fig. S15, A and B). The proportion of hDEGs near HARs and hCONDELs is highest for non-neuronal consensus types such as VLMCs (VLMC\_1), microglia (Micro-PVM\_1), and oligodendrocytes (Oligo\_1), likely owing to the larger intronic and flanking intergenic regions of hDEGs in these cell types (fig. S15D). We found some enrichment of HARs and hCONDELs near NHP-specific DEGs (fig. S16), which supports previous findings that show that accelerated genomic regions in different primate lineages cluster near similar genes (48).

By contrast, HAQERs are not enriched near hDEGs in any consensus cell type (fig. S15C). Unlike HARs and hCONDELs, HAQERs need not be conserved across other species and potentially include genomic regions that were previously nonfunctional but that acquired new functions in humans. Therefore, we tested whether HAQERs were enriched near genes with differential expression between humans and chimpanzees, without regard for their expression in other primates, and found significant enrichment for the OPC and L5/6 IT *CAR3* subclasses (fig. S17). HARs and hCONDELs are also enriched near genes with differential expression between humans and chimpanzees in multiple cell subclasses, reflecting the enrichment of HARs and hCONDELs near hDEGs.

Because hDEGs are highly enriched for synaptic genes (Fig. 5D), we asked whether a subset of hDEGs that are near HARs or hCONDELs and are potentially adaptive are associated with specialized localizations or molecular functions of the synapse. By performing gene set enrichment analysis using SynGO (28), we found a significant enrichment of hDEGs among SynGO genes compared with all expressed genes ( $P < 10^{-16}$ ) and a further enrichment of hDEGs near HARs and hCONDELs among SynGO genes compared with all hDEGs ( $P < 10^{-5}$ ) (Fig. 6B, fig. S18, and table S8). Among the most-enriched SynGO terms were synapse assembly, synaptic membrane organization, and trans-synaptic signaling. Other SynGO terms were not enriched, including synaptic transport, metabolism, cytoskeleton, and vesicle exocytosis machinery (Fig. 6B, figs. S18 and S19, and table S8). We also found a significant enrichment of hDEGs, and those near HARs and hCONDELs, within gene families that encode synaptic adhesion molecules ( $P < 10^{-6}$ ) (Fig. 6C, figs. S20 and S21, and table S8).

We next examined how synaptic genetic programs have changed expression in specific human consensus types. Some gene families (neurexins, interleukin receptors, FLRT proteins, and Trk receptors) mainly changed in excitatory types in deep cortical layers, whereas other families (neuroligins, protocadherins, latrophilins, and immunoglobulin superfamily DCC re-

ceptors) primarily changed in inhibitory types (Fig. 6C and fig. S20). *PVALB* interneurons and deep-layer excitatory neurons are known to establish specific microcircuits in deeper cortical layers (49), and those types show complementary expression changes in ephrin ligands and receptors, respectively (Fig. 6C and fig. S20B). Moreover, although teneurins, PTP receptors, and EPH receptors include hDEGs in almost all consensus types (Fig. 6C), specific family members are hDEGs only in a subset of types. For instance, 13 genes within these families (*EPHA3*, *EPHA4*, *EPHA5*, *EPHA7*, *EPHB6*, *PTPRF*, *PTPRG*, *PTPRK*, *PTPRQ*, *PTPRS*, *PTPRT*, *PTPRU*, and *TENM3*) changed expression in only one or two consensus types within the 14 consensus types of L5/6 excitatory neurons (Fig. 6D and figs. S20B and S22, A and B). Similarly, several genes (*CDH1*, *CDH2*, *CDH24*, *EFNA5*, *EFNB2*, *IGSF9B*, *LGI1*, *LGI2*, *LRFN5*, and *SLTRK4*) that only diverged in expression in inhibitory interneurons also showed selective changes in only one or two consensus types (figs. S20B and S22C). Taken together, our data highlight human specializations of synaptic gene programs that are highly localized to specific cell types and may underlie differences in synaptic connectivity in specific microcircuits.

We leveraged existing data to identify human-specific sequence changes in regulatory regions linked to hDEGs that may drive differential expression in select cell types. For example, *PTPRG* is a member of the PTP receptor family that acts as presynaptic organizers for synapse assembly (50). Genetic variants in *PTPRG* have been associated with neuropsychiatric disorders, and *Ptprg* mutant mice show memory deficits, supporting an important role for *PTPRG* in cognitive function (51–54). We found that *PTPRG* was widely expressed across cell types (fig. S23A) and had lower expression in humans than in NHPs in four consensus types: one excitatory neuron type (L5 ET\_2), microglia (Micro-PVM\_1), and two inhibitory neuron types (VIP\_2 and VIP\_6) (Fig. 6E and fig. S23B). *PTPRG* is located near HARsv2\_1818 (chr3:61283266–61283416, hg38), which has decreased enhancer activity from the human sequence compared with that from the orthologous chimpanzee sequence (14). Of note, a 5-kb genomic interval that includes HARsv2\_1818 has been shown to interact with the promoter of *PTPRG*, specifically in excitatory neurons but not in inhibitory neurons or microglia (15, 16). This raises the possibility that decreased enhancer activity from HARsv2\_1818 in humans may have decreased *PTPRG* expression specifically in the excitatory neuron consensus type L5 ET\_2 and that separate regulatory mechanisms may decrease *PTPRG* expression in microglia and specific inhibitory neuron consensus types. In support of this hypothesis, there is a base-pair substi-

tution in the human HARsv2\_1818 sequence that removes a binding site for TWIST1, a basic helix-loop-helix transcription factor. We found that *TWIST1* is expressed predominantly in excitatory neuron consensus type L5 ET\_2 compared with microglia or inhibitory neuron consensus types (Fig. 6E and fig. S23C), further suggesting that human-specific sequence changes in HARsv2\_1818 may specifically decrease *PTPRG* expression in L5 ET\_2. We extended this analysis to link 112 HARs to 92 hDEGs in neurons using existing data (15, 16), and we posit that genomic interaction data from specific cell types may reveal additional genes that may be regulated by human-specific sequence changes.

## Discussion

Transcriptomic profiling of more than 570,000 nuclei from the MTG region of primate neocortex reveals a notably conserved cellular architecture across humans and four NHPs: chimpanzees, gorillas, macaques, and marmosets. Humans and the other great apes have nearly identical proportions and laminar distributions of consensus types, whereas marmosets are the most distinct, with markedly increased proportions of L5 ET and L5/6 IT *CAR3* excitatory neurons and Chandelier interneurons. Great apes have similar proportions of two major subtypes of L5/6 IT *CAR3* neurons that have high or low *CUX2* expression and distinct positions in layers 5 and 6, and marmosets have mostly high-*CUX2* neurons. Unlike those in primates, L5/6 IT *CAR3* neurons in mice express markers of both subtypes. These neurons are transcriptomically homogeneous across the mouse cortex yet project to diverse cortical targets, including proximal areas and homotopic areas in the contralateral hemisphere (55). High-*CUX2* neurons are selectively enriched in language-related regions in the human temporal and parietal cortex (MTG, A1, and ANG) (21), and these neurons may have distinct connectivity and contribute to the functional specializations of these regions.

Cell-type expression differences are more pronounced than proportion differences and mostly parallel evolutionary distances. One notable exception is that neuronal expression diverged more rapidly in the human lineage (56) than in the chimpanzee and gorilla lineages. In all primates, evolutionary expression changes are substantially accelerated in microglia, astrocytes, and oligodendrocytes compared with neurons and OPCs, even after accounting for higher variability of glial expression between individuals. In addition, human glia express more highly divergent genes than chimpanzee or gorilla glia, suggesting faster divergence of human microglia and astrocytes (9) as well as oligodendrocytes (8) among great apes. Finally, we observed human-specific changes in isoform usage of genes that often have conserved transcript

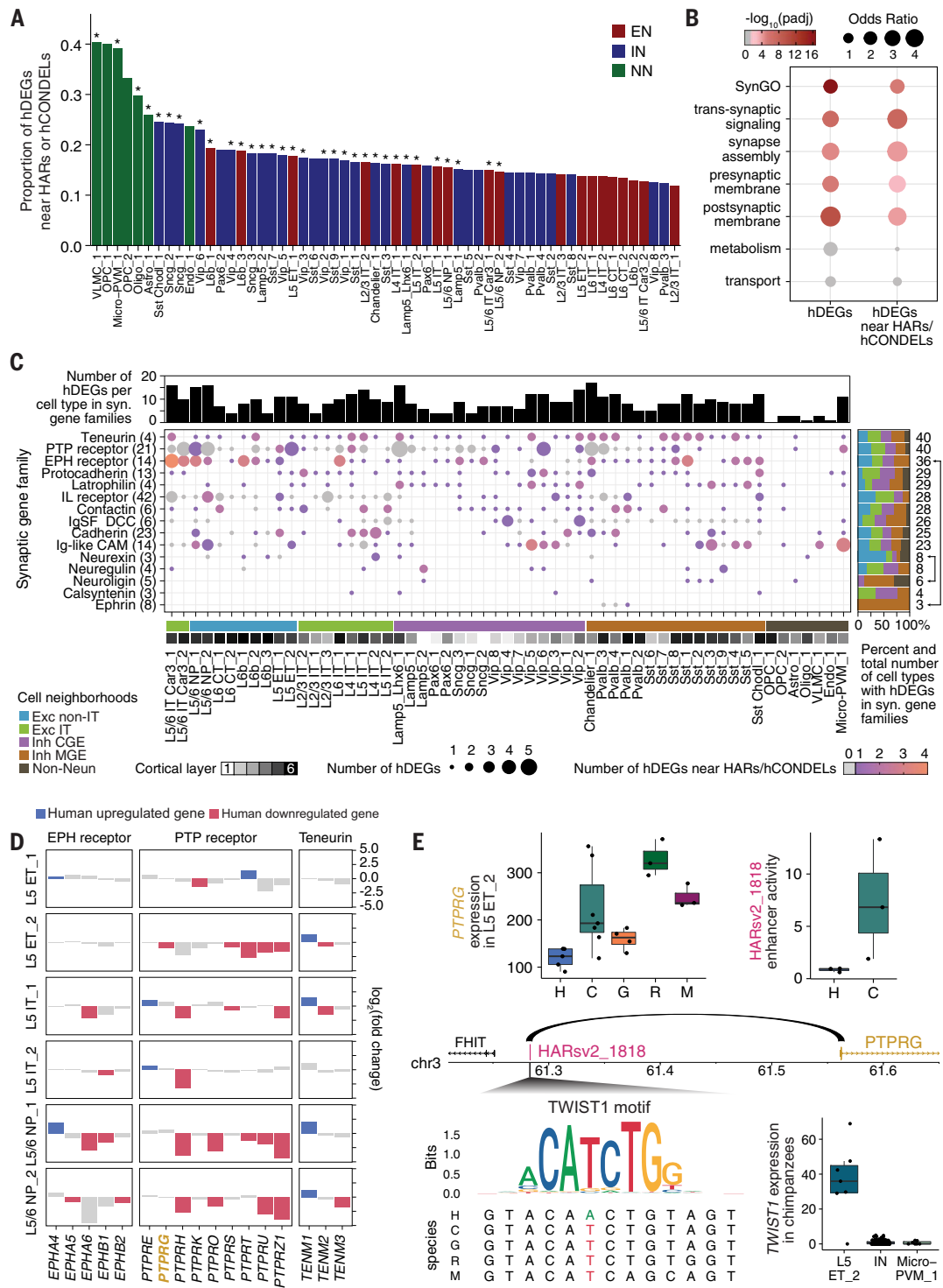


**Fig. 6. HARs and hCONDELs are enriched near hDEGs.** (A) Asterisks indicate HARs and hCONDELs that are enriched near hDEGs in specific consensus cell types at 5% FDR. EN, excitatory neuron; IN, inhibitory neuron; NN, non-neuronal. (B) hDEGs, as well as hDEGs near HARs or hCONDELs, are enriched for genes annotated in specific SynGO terms (28). Nonsignificant associations are in gray. (C) Synaptic gene families with highly divergent expression patterns. The brackets on the far right highlight examples of synaptic gene families with transsynaptic interactions that show human differential gene expression in cell types known to form canonical cortical circuits. (D) Patterns of expression

change between humans and NHPs for three highly divergent families in consensus types of L5 excitatory neurons. EPH, ephrin; PTP, protein tyrosine phosphatase. (E) PTPRG has decreased expression in human L5 ET\_2 (each point represents normalized pseudobulk gene expression per individual). Its promoter interacts with the intergenic region containing HARsv2\_1818 (16), which has decreased enhancer activity in human SH-SY5Y cells (14). A base-pair change in the human HARsv2\_1818 sequence removes a potential binding site for TWIST1, which is highly expressed in L5 ET\_2. For the box plots, the center line represents the median, box limits are upper and lower quartiles, and whiskers are minimum and maximum values.

amounts. This highlights the importance of profiling full-length transcripts in molecular studies of cellular diversity to identify a more comprehensive set of genes with potentially functional changes.

Humans and NHPs have hundreds of DEGs that are specific to one or a few consensus cell types and are enriched in molecular pathways related to ribosomal processing, cell connectivity, and synaptic function. Human-specific changes in synaptic gene expression are complex, and distinct families of genes are differentially expressed in select neuronal and non-neuronal cell types. For example, ephrin molecules specifically differ in *PVALB* inhibitory cell types, whereas their cognate receptors (EPH receptors) change prominently in deep layer excitatory neurons. Importantly, ephrin-EPH receptor signaling has been shown to promote synaptogenesis in the mouse developing cortex (57, 58). Because *PVALB* interneurons and excitatory neurons form cell type–specific patterns of connectivity (49), the differential expression of ephrins and EPH receptors could reflect primate species differences in the formation of inhibitory microcircuits that involve specific subtypes of *PVALB* interneurons and excitatory neurons. Also, a substantial proportion of synaptic cell-adhesion genes showed downregulated expression in human neurons, particularly in gene families that encode PTP receptors, including PTPRG, and EPH receptors. Some studies have proposed roles in synapse elimination for members of highly divergent synaptic families, including Pedh10, ephrin-B1, and ephrin-A2 (59, 60). In such a case, reduced expression of negative regulators of synaptic assembly in human neurons could lead to an enhanced ability to form synaptic connections, potentially underlying the greater number of synapses per neuron that are observed in the human cortex compared with that of NHPs (61).

Emerging evidence demonstrates the critical role that non-neuronal cell types play in cortical development, network function, and behavior (62–67). Previous molecular assays have identified a role for ErbB4-mediated signaling in astrogenesis, astrocyte-neuron communication, and astrocyte-induced neuronal remodeling, potentially through both paracrine and autocrine signaling (68–70). We observed changes in the expression of the *ERBB4* receptor and its cognate ligands *NRG2* and *NRG3* in human astrocytes compared with chimpanzee and gorilla astrocytes. Altogether, these findings point toward finely regulated molecular specializations underlying neuronal and glial communication in the human cortex. Our data also serve as a resource for future investigation of human-enriched astrocyte and microglia gene programs associated with disease.

Deeper sampling of cells and individuals will be needed to disentangle the genetic and

environmental effects that drive cell-type specializations and whether expression differences represent changes in cell types or cell states. Moreover, molecular and morphological specializations of human cortical neurons may be linked to macroscale anatomical changes given that the number of synapses per neuron increases predictably with brain size across human and non-human primates (71). Thus, a phylogenetically broader set of mammals, including large-brained, nonprimate species, will be needed to differentiate between cellular features that result from human brain scaling versus specialized cognitive capacities, such as language.

Cell type–specific evolutionary changes in gene expression are likely driven by sequence changes to regulatory regions that can be active with high spatial and temporal precision. This is supported by prior studies of genome-sequence evolution in humans and other species that estimated that more than 80% of adaptive sequence change is likely regulatory (45, 72, 73). Indeed, we find that previously identified genomic regions that have human-specific sequence changes, such as HARs and hCONDELS, are enriched near hDEGs. This association is observed for both neuronal and non-neuronal consensus types. In addition to well-described changes in the number and function of neurons in the human brain (74), many non-neuronal cell types also undergo comparable changes in the human lineage (75, 76). Moreover, hDEGs, including those near HARs and hCONDELS, have been found to play critical roles in synapse establishment, elimination, and maintenance when expressed by neuronal and non-neuronal cells (77). Associating genomic regions with signatures of selection in humans to hDEGs provides a framework to link regulatory sequence changes to human-specific cellular and circuit-level phenotypes through expression changes in select cell types.

## Materials and methods

### Tissue specimens from primate species

#### Human postmortem tissue specimens

Deidentified postmortem adult human brain tissue was obtained after receiving permission from the deceased's next of kin. Tissue collection was performed in accordance with the provisions of the United States Uniform Anatomical Gift Act of 2006 described in the California Health and Safety Code section 7150 (effective 1 January 2008) and other applicable state and federal laws and regulations. The Western Institutional Review Board reviewed tissue collection procedures and determined that they did not constitute human subject research requiring institutional review board (IRB) review.

Male and female individuals 18 to 68 years of age with no known history of neuropsychiatric

or neurological conditions were considered for inclusion in the study. Routine serological screening for infectious disease (HIV, hepatitis B, and hepatitis C) was conducted using individual blood samples, and individuals testing positive for infectious disease were excluded from the study.

Specimens were screened for RNA quality and samples with average RNA integrity (RIN) values  $\geq 7.0$  were considered for inclusion in the study. Postmortem brain specimens were processed as previously described (17) ([dx.doi.org/10.17504/protocols.io.bf4ajqse](https://doi.org/10.17504/protocols.io.bf4ajqse)). Briefly, coronal brain slabs were cut at 1-cm intervals, frozen in dry-ice-cooled isopentane, and transferred to vacuum-sealed bags for storage at  $-80^{\circ}\text{C}$  until the time of further use. To isolate the MTG, tissue slabs were briefly transferred to  $-20^{\circ}\text{C}$ , and the region of interest was removed and subdivided into smaller blocks on a custom temperature controlled cold table. Tissue blocks were stored at  $-80^{\circ}\text{C}$  in vacuum-sealed bags until later use.

#### Chimpanzee and gorilla tissue specimens

Chimpanzee tissue was obtained from the National Chimpanzee Brain Resource (supported by NIH grant NS092988). Gorilla samples were collected postmortem after naturally occurring death or euthanasia of the animals for medical conditions at various zoos. Gorilla and chimpanzee brains were divided into 2-cm coronal slabs, flash-frozen using dry-ice-cooled isopentane, liquid nitrogen, or a  $-80^{\circ}\text{C}$  freezer, and then stored in freezer bags at  $-80^{\circ}\text{C}$ . Tissues from the MTG were removed from appropriate slabs, which were maintained on dry ice during dissection and were shipped to the Allen Institute overnight on dry ice.

#### Macaque tissue specimens

Macaque tissue samples were obtained from the University of Washington National Primate Resource Center under a protocol approved by the University of Washington Institutional Animal Care and Use Committee. Immediately after euthanasia, macaque brains were removed and transported to the Allen Institute in artificial cerebral spinal fluid equilibrated with 95%  $\text{O}_2$  and 5%  $\text{CO}_2$ . Upon arrival at the Allen Institute, brains were divided down the midline, and each hemisphere was subdivided coronally into 0.5-cm slabs.

Slabs were flash frozen in dry-ice-cooled isopentane, transferred to vacuum-sealed bags, and stored at  $-80^{\circ}\text{C}$ . MTG was removed from brain slabs as described above for human tissues.

#### Marmoset tissue specimens

Marmoset experiments were approved by and in accordance with Massachusetts Institute of Technology IACUC protocol number 051705020. Adult marmosets (1.5 to 2.5 years old, three

individuals) were deeply sedated by intramuscular injection of ketamine (20 to 40 mg kg<sup>-1</sup>) or alfaxalone (5 to 10 mg kg<sup>-1</sup>), followed by intravenous injection of sodium pentobarbital (10 to 30 mg kg<sup>-1</sup>). When the pedal withdrawal reflex was eliminated and/or the respiratory rate was diminished, animals were transcardially perfused with ice-cold sucrose-HEPES buffer (78). Whole brains were rapidly extracted into fresh buffer on ice. Sixteen 2-mm coronal blocking cuts were rapidly made using a custom-designed marmoset brain matrix. Slabs were transferred to a dish with ice-cold dissection buffer (78). All regions were dissected using a marmoset atlas as reference (79), and were snap-frozen in liquid nitrogen or dry ice-cooled isopentane, and stored in individual microcentrifuge tubes at -80°C.

Temporal lobe dissections targeted area TE3 and TPO on the lateral temporal surface. Though a true homology to catarhine MTG may not exist in marmosets, these areas in marmoset form part of the temporal lobe association cortex. Moreover, on the basis of tract tracing connectivity studies (80), TE3 and TPO participate in the “default mode network,” a functionally coupled network of higher-order association cortex that includes MTG in other species (81). Cortical area DLPFC targeted the dorsolateral surface of PFC, approximately 2.5 to 3 mm from the frontal pole. ACC/PFCm included medial frontal cortex anterior to the genu of the corpus callosum. M1 dissections were stained with fluorescent Nissl and targeted the hand or trunk region. S1 like sampled all primary somatosensory areas (A3,A1/2). A1 dissections targeted primary auditory area but likely include some rostral and caudal parabelt cortex. V1 dissections were collected on the dorsal bank of the calcarine sulcus approximately 4 to 6 mm from the posterior pole.

#### Tissue processing and snRNA-seq

##### SMART-seq v4 nucleus isolation and sorting (human, chimpanzee, and gorilla)

Vibratome sections of MTG blocks were stained with fluorescent Nissl permitting microdissection of individual cortical layers as previously described ([dx.doi.org/10.17504/protocols.io.bq6ymzfw](https://doi.org/10.17504/protocols.io.bq6ymzfw)). Nucleus isolation was performed as described ([dx.doi.org/10.17504/protocols.io.ztqf6mw](https://doi.org/10.17504/protocols.io.ztqf6mw)).

Briefly, single-nucleus suspensions were stained with DAPI (4,6-diamidino-2-phenylindole dihydrochloride, ThermoFisher Scientific, D1306) at a concentration of 0.1 µg/ml. Controls were incubated with mouse IgGk-PE Isotype control (BD Biosciences, 555749, 1:250 dilution) or DAPI alone. To discriminate between neuronal and non-neuronal nuclei, samples were stained with mouse anti-NeuN conjugated to PE (FCMAB317PE, EMD Millipore) at a dilution of 1:500. Single-nucleus sorting was carried out on either a BD FACSaria II SORP or BD FACSaria Fusion instrument (BD Biosciences) using a 130-µm

nozzle and BD Diva software v8.0. A standard gating strategy based on DAPI and NeuN staining was applied to all samples as previously described (17). Doublet discrimination gates were used to exclude nuclei multiplets. Individual nuclei were sorted into 96-well plates, briefly centrifuged at 1000 rpm, and stored at -80°C.

#### SMART-seq v4 RNA-seq

The SMART-Seq v4 Ultra Low Input RNA Kit for Sequencing (Takara no. 634894) was used per the manufacturer's instructions. Standard controls were processed with each batch of experimental samples as previously described. After reverse transcription, cDNA was amplified with 21 PCR cycles. The NexteraXT DNA Library Preparation (Illumina FC-131-1096) kit with NexteraXT Index Kit V2 Sets A-D (FC-131-2001, 2002, 2003, or 2004) was used for sequencing library preparation. Libraries were sequenced on an Illumina HiSeq 2500 instrument (Illumina HiSeq 2500 System, RRID: SCR\_016383) using Illumina High Output V4 chemistry. The following instrumentation software was used during data generation workflow: SoftMax Pro v6.5; VWorks v11.3.0.1195 and v13.1.0.1366; Hamilton Run Time Control v4.4.0.7740; Fragment Analyzer v1.2.0.11; and Mantis Control Software v3.9.7.19.

#### SMART-seq v4 gene expression quantification

For human, raw read (fastq) files were aligned to the GRCh38 genome sequence (Genome Reference Consortium, 2011) with the RefSeq transcriptome version GRCh38.p2 (RefSeq, RRID:SCR\_003496, current as of 13 April 2015) and updated by removing duplicate Entrez gene entries from the gtf reference file for STAR processing, as previously described (17). For chimpanzee and gorilla, the Clint\_PTRv2 and Susie3 NCBI reference genomes were used for alignment, respectively. For alignment, Illumina sequencing adapters were clipped from the reads using the fastqMCF program (from ea-utils).

After clipping, the paired-end reads were mapped using Spliced Transcripts Alignment to a Reference (STAR v2.7.3a, RRID:SCR\_015899) using default settings. Reads that did not map to the genome were then aligned to synthetic construct (i.e., ERCC) sequences and the *Escherichia coli* genome (version ASM584v2). Quantification was performed using summarizeOverlaps from the R package GenomicAlignments v1.18.0. Gene expression was calculated as counts per million (CPM) of exonic plus intronic reads.

#### 10x RNA-seq (human, chimpanzee, gorilla, and macaque)

Nucleus isolation for 10x Chromium snRNA-seq was conducted as described ([dx.doi.org/10.17504/protocols.io.y6rfzd6](https://doi.org/10.17504/protocols.io.y6rfzd6)).

Gating was as described for SSv4 above. NeuN<sup>+</sup> and NeuN<sup>-</sup> nuclei were sorted into separate tubes and were pooled at a defined ratio (90% NeuN<sup>+</sup>, 10% NeuN<sup>-</sup>) after sorting. Sorted samples were centrifuged, frozen in a solution of 1X PBS, 1% BSA, 10% DMSO, and 0.5% RNAsin Plus RNase inhibitor (Promega, N2611), and stored at -80°C until the time of 10x chip loading.

Immediately before loading on the 10x Chromium instrument, frozen nuclei were thawed at 37°C, washed, and quantified for loading as described ([dx.doi.org/10.17504/protocols.io.nx3dfqn](https://doi.org/10.17504/protocols.io.nx3dfqn)). Samples were processed using the 10x Chromium Single-Cell 3' Reagent Kit v3 following the manufacturer's protocol. Gene expression was quantified using the default 10x Cell Ranger v3 (Cell Ranger, RRID:SCR\_017344) pipeline.

Reference genomes included the modified genome annotation described above for SMART-seq v4 quantification (human, Clint\_PTRv2 (chimpanzee), Susie3 (gorilla), and Mmul\_10 (rhesus macaque). Introns were annotated as “mRNA,” and intronic reads were included in expression quantification.

#### 10x RNA-seq (marmoset)

Unsorted single-nucleus suspensions from frozen marmoset samples were generated as in (10). GEM generation and library preparation were performed following the manufacturer's protocol (10X Chromium single-cell 3' v.3, protocol version #CG000183\_ ChromiumSingle-Cell3'\_v3\_UG\_Rev-A). Raw sequencing reads were aligned to the CJ1700 reference. Reads that mapped to exons or introns were assigned to annotated genes.

#### RNA-seq processing and clustering

##### Cell-type label transfer

Human MTG and M1 reference taxonomy subclass labels (12, 21) were transferred to nuclei in the current MTG dataset using Seurat's label transfer (3000 high variance genes using the “vst” method then filtered through exclusion list). For human label mapping to other species, higher variance genes were included from a list of orthologous genes [14,870 genes; downloaded from NCBI Homologene (<https://www.ncbi.nlm.nih.gov/homologene>) in November 2019; RRID SCR\_002924]. This was carried out for each species and RNA-seq modality dataset; for example, human-Cv3 and human-SSv4 were labeled independently. Each dataset was subdivided into five neighborhoods—IT and non-IT excitatory neurons, CGE- and MGE-derived interneurons, and non-neuronal cells—based on marker genes and transferred subclass labels from published studies of human and mouse cortical cell types and cluster grouping relationships in a reduced dimensional gene expression space. MTG and M1 subclass labels were highly consistent for all neighborhoods and species

(adjusted Rand index 0.88 to 0.99), and a final set of labels was manually curated using additional information, such as layer dissections.

#### Filtering low-quality nuclei

SSv4 nuclei were included for analysis if they passed all QC criteria:

- >30% cDNA longer than 400 base pairs
- >500,000 reads aligned to exonic or intronic sequence
- >40% of total reads aligned
- >50% unique reads
- >0.7 TA nucleotide ratio

QC was then performed at the neighborhood level. Neighborhoods were integrated together across all species and modality; for example, deep excitatory neurons from human-Cv3, human- SSv4, Chimp-Cv3, and so on. datasets were integrated using Seurat integration functions with 2000 high variance genes from the orthologous gene list. Integrated neighborhoods were Louvain clustered into over 100 meta cells, and low-quality meta cells were removed from the dataset based on relatively low UMI or gene counts (which included glia and neurons with more than 500 and 1000 genes detected, respectively), predicted doublets using DoubletFinder (82) and default parameters (included nuclei with doublet scores under 0.3), and/or subclass label prediction metrics within the neighborhood (i.e., excitatory labeled nuclei that clustered with majority inhibitory or non-neuronal nuclei).

#### RNA-seq clustering

Nuclei were normalized using SCTransform (19), and neighborhoods were integrated together within a species and across individuals and modalities by identifying mutual nearest neighbor anchors and applying canonical correlation analysis as implemented in Seurat (18). For example, deep excitatory neurons from human-Cv3 were split by individual and integrated with the human-SSv4 deep excitatory neurons. Integrated neighborhoods were Louvain clustered into more than 100 meta cells. Meta cells were then merged with their nearest neighboring meta cell until merging criteria were sufficed, which is a split and merge approach that has been previously described (12). The remaining clusters underwent further QC to exclude low-quality and outlier populations. These exclusion criteria were based on irregular groupings of metadata features that resided within a cluster.

#### Robustness tests of cell subclasses using MetaNeighbor

MetaNeighbor v1.12 (38, 39) was used to provide a measure of neuronal and non-neuronal subclass and cluster replicability within and across species. We subset snRNA-seq datasets from each species to the list of common orthologs before further analysis. For each assess-

ment, we identified highly variable genes using the get\_variable\_genes function from MetaNeighbor. To identify homologous cell types, we used the MetaNeighborUS function, with the fast\_version and one\_vs\_best parameters set to TRUE. The one\_vs\_best parameter identifies highly specific cross-dataset matches by reporting the performance of the closest neighboring cell type over the second closest as a match for the training cell type, and the results are reported as the relative classification specificity (AUROC). This step identified highly replicable cell types within each species and across each species pair. All 24 subclasses are highly replicable within and across species (one\_vs\_best AUROC of 0.96 within species and 0.93 across species in fig. S4A).

#### Defining cross-species consensus cell types

Although cell type clusters are highly replicable within each species (one\_vs\_best AUROC of 0.93 for neurons and 0.87 for non-neurons), multiple transcriptionally similar clusters mapped to each other across each species pair (average cross-species one\_vs\_best AUROC of 0.76). To build a consensus cell type taxonomy across species, we defined a cross-species cluster as a group of clusters that are either reciprocal best hits or clusters with AUROC > 0.6 in the one\_vs\_best mode in at least one pair of species. This lower threshold (AUROC > 0.6) reflects the high difficulty and/or specificity of testing only against the best performing other cell type. We identified 86 cross-species clusters, each containing clusters from at least two primates. Any unmapped clusters were assigned to one of the 86 cross-species clusters based on their transcriptional similarity. For each unmapped cluster, the top 10 of their closest neighbors were identified using MetaNeighborUS one\_vs\_all cluster replicability scores, and the unmapped cluster was assigned to the cross-species cluster in which a strict majority of its nearest neighbors belong. For clusters with no hits, this was repeated using the top-20 closest neighbors, still requiring a strict majority to assign a cross-species type. Five hundred ninety-four clusters present in five primates (i.e., union) mapped to 86 cross-species clusters, with 493 clusters present across 57 consensus cross-species clusters shared by all five primates (table S6). This is described in more detail in our companion manuscript (83). Additional sampling of species and developmental time points will be needed to distinguish between transcriptomic specializations of conserved cell types and the emergence of closely related but distinct cell types. In this study, the 101 clusters with initial homologies across fewer than five species were assigned to the most similar of the 57 consensus types.

An alternative approach for consensus clustering was used to assess the robustness of homologous cell type clusters identified by

MetaNeighbor. For each of the five cell-type neighborhoods (non-neuronal, MGE- and CGE-derived interneurons, and IT- and non-IT-projecting excitatory neurons), we built a reference with four primate datasets as query for cell type annotation using scArches (40). We built each reference dataset using 2000 highly variable genes, trained a model on the reference using scPoli (84), and mapped the query cells onto the reference data (fig. S12). scPoli learns a set of cell-type prototypes from the latent cell representation of the reference data (fig. S12, C and D). The cells in the query dataset were annotated based on their closest cell-type prototype in the reference data (fig. S12E), and the classification uncertainty was estimated by Euclidean distance from this prototype (fig. S12F). Query cells typically mapped to cell-type prototypes identified in the reference data with low label transfer uncertainty, highlighting the robustness of the primate MTG consensus taxonomy. Cell-type labels predicted by scPoli were largely consistent with the consensus cell types identified by MetaNeighbor (overall classification accuracy with scPoli = 0.74, average cell-type classification accuracy = 0.68), although the classification accuracy varied with cell-type neighborhood (ranging from 0.91 across glial cell types to 0.69 across IT-type excitatory neurons).

#### Cell-type taxonomy generation

For each species, a taxonomy was built using the final set of clusters and was annotated using subclass mapping scores, dendrogram relationships, marker gene expression, and inferred laminar distributions. Within-species taxonomy dendograms were generated using build\_dend function from scratch\_hicat R package. A matrix of cluster median log<sub>2</sub>(CPM + 1) expression across the 3000 High-variance genes for Cv3 nuclei from a given species were used as input. The cross-species dendrogram was generated with a similar workflow but was down-sampled to a maximum of 100 nuclei per cross-species cluster per species. The 3000 High-variance genes used for dendrogram construction were identified from the down-sampled matrix containing Cv3 nuclei from all five species. We generated the complete cross-species cluster dendrogram using average-linkage hierarchical clustering with (1 - average MetaNeighborUS one\_vs\_all cluster replicability scores) for each pair of 86 cross-species clusters as a measure of distance between cell types.

#### Cell-type comparisons across species

##### Differential gene expression

To identify subclass marker genes within a species, Cv3 datasets from each species were down-sampled to a maximum of 100 nuclei per cluster per individual.

Differentially expressed marker genes were then identified using the FindAllMarkers function from Seurat, using the Wilcoxon rank-sum test on log-normalized matrices with a maximum of 500 nuclei per group (subclass versus all other nuclei as background). Statistical thresholds for markers are indicated in their respective figures. To identify species marker genes across subclasses and consensus cell types, Cv3 datasets from each species were down-sampled to a maximum of 50 nuclei per cluster per individual. Down-sampled counts matrices were then grouped into pseudo-bulk replicates (species, individual, subclass or consensus types) and the counts were summed per replicate. DESeq2 functionality was then used to perform a differential expression analysis between species pairs (or comparisons of interest) for each subclass or consensus type using the Wald test statistic.

#### Expression correlations

Subclasses were compared between each pair of species using Spearman correlations on subclass median  $\log_2(CPM + 1)$  expression of orthologous genes that had a median value greater than zero in both species. These Spearman correlations were then visualized as heatmaps and also compared to the human-centric evolutionary distance from each species in Fig. 2. Similarly, subclasses were compared across individuals within each species, and the average Spearman correlation of all pairwise comparisons of individuals was calculated. Within species correlations were performed on orthologous genes with median values greater than zero in all donors for a given subclass. Nuclei were down-sampled to a maximum of 100 nuclei per subclass per donor for comparisons.

#### Taxonomy comparisons

To assess homologies between clusters from taxonomies of different species or different studies, we constructed Euclidean distance heatmaps that were anchored on one side by the taxonomies' dendrogram. The heatmaps display the cluster labels of a single taxonomy on either end, and the heatmap values represent the Euclidean distance between cluster centroids in the reduced dimensional space using 30 to 50 principal components from a PC analysis. In the case of cross-species comparisons, the reduced space was derived from Cv3 data. The  $-\log_{10}$ (Euclidean distance) is plotted, with smaller values indicating more similar transcriptomic profiles.

#### Estimating differential isoform usage between great apes

We used Smart-seq snRNA-seq data from humans (~14,500 cells), chimpanzees (~3500 cells), and gorillas (~4300 cells) to assess isoform switching between the species for each cell subclass. The RNA-seq reads were mapped

to each species' genome using STAR as described above. The isoforms were quantified using RSEM on a common set of annotated transcripts (TransMap V5 downloaded from the UCSC browser, RRID:SCR\_005780) by aggregating reads from cells in each cell subtype using a pseudo-bulk method:

1. Aggregated reads from cells in each subclass
2. Mapped reads to the human, chimpanzee, or gorilla reference genome with STAR 2.7.7a using default parameters
3. Transformed genomic coordinates into transcriptomic coordinates using STAR parameter:–quantMode TranscriptomeSAM
4. Quantified isoform and gene expression using RSEM v1.3.3 parameters (RSEM, RRID: SCR\_013027):–bam–seed 12345–paired-end-forward-prob 0.5–single-cell- prior=calc-ci

The isoform proportion metric (isoP) was defined as the isoform expression [transcripts per million (TPM)] normalized by the total expression of the gene the isoform belongs to. To focus on highly expressed genes, we considered only isoforms originating from the top 50% (ranked by gene expression) of genes for each species. To control the variability of isoP values, we derived the 80% confidence intervals by comparing the isoP values of different donors for each species using the following procedure:

1. The isoP values (ranging from 0 to 1) for donor 1 are binned into 10 bins of size 0.1.
2. The isoforms in each bin are sorted by the isoP values in donor 2.
3. The lower and upper bounds of the 80% isoP confidence interval are defined as 10% and 90% percentile of this sorted list.
4. The procedure was repeated, switching donors 1 and 2, and the isoP confidence interval bounds values from the two calculations were averaged.

The isoform switching between species was considered significant for isoforms whose confidence intervals were nonoverlapping. We defined cross-species isoform switches as those that involved a major isoform in one of the species (i.e., isoP > 0.5) and report them in table S4. A subset of isoforms with strong cross-species switching were identified that had isoP > 0.7 in one species, isoP < 0.1 in the other species, and >3-fold change in proportions between the species.

#### Identifying changes in cell-type proportions across species

Cell-type proportions are compositional, where the gain or loss of one population necessarily affects the proportions of the others, so we used scCODA (43) to determine which changes in cell class, subclass, and cluster proportions across species were statistically significant. We focused these analyses on neuronal populations because these were deeply sampled in all five species based on sorting of nuclei with NeuN immunostaining. The proportion

of each neuronal class, subclass, and cluster was estimated using a Bayesian approach where proportion differences across individuals were used to estimate the posterior. All compositional and categorical analyses require a reference population against which to evaluate differences, and because we were uncertain which populations should be unchanged, we iteratively used each cell type and each species as a reference when computing abundance changes. To account for sex differences, we included it as a covariate when testing for abundance changes. We report the effect size of each species and sex for each cell subclass and used a mean inclusion probability cutoff of 0.7 for calling a population credibly different.

#### In situ profiling of gene expression

##### MERFISH data collection

Human postmortem frozen brain tissue was embedded in Optimum Cutting Temperature medium (VWR, 25608-930) and sectioned on a Leica cryostat at  $-17^{\circ}\text{C}$  at 10  $\mu\text{m}$  onto Vizgen MERSCOPE coverslips (VIZGEN 2040003). These sections were then processed for MERSCOPE imaging according to the manufacturer's instructions. Briefly, sections were allowed to adhere to these coverslips at room temperature for 10 min before a 1-min wash in nuclease-free phosphate buffered saline (PBS) and fixation for 15 min in 4% paraformaldehyde in PBS. Fixation was followed by three 5-min washes in PBS before a 1-min wash in 70% ethanol. Fixed sections were then stored in 70% ethanol at  $4^{\circ}\text{C}$  before use and for up to one month. Human sections were photobleached using a 150-W LED array for 72 hours at  $4^{\circ}\text{C}$  before hybridization then washed in 5 ml of Sample Prep Wash Buffer (VIZGEN 20300001) in a 5-cm petri dish. Sections were then incubated in 5 ml of Formamide Wash Buffer (VIZGEN 20300002) at  $37^{\circ}\text{C}$  for 30 min. Sections were hybridized by placing 50  $\mu\text{l}$  of VIZGEN-supplied Gene Panel Mix onto the section, covering with parafilm, and incubating at  $37^{\circ}\text{C}$  for 36 to 48 hours in a humidified hybridization oven.

After hybridization, sections were washed twice in 5 ml of Formamide Wash Buffer for 30 min at  $47^{\circ}\text{C}$ . Sections were then embedded in acrylamide by polymerizing VIZGEN Embedding Premix (VIZGEN 20300004) according to the manufacturer's instructions. Sections were embedded by inverting sections onto 110  $\mu\text{l}$  of Embedding Premix and 10% Ammonium Persulfate (Sigma A3678) and TEMED (BioRad 161-0800) solution applied to a Gel Slick (Lonza 50640) treated 2-inch-by-3-inch glass slide. The coverslips were pressed gently onto the acrylamide solution and allowed to polymerize for 1.5 hours. After embedding, sections were cleared for 24 to 48 hours with a mixture of VIZGEN Clearing Solution (VIZGEN 20300003) and Proteinase K (New England Biolabs P8107S) according to the manufacturer's instructions.

After clearing, sections were washed twice for 5 min in Sample Prep Wash Buffer (PN 20300001).

VIZGEN DAPI and PolyT Stain (PN 20300021) were applied to each section for 15 min followed by a 10-min wash in Formamide Wash Buffer. Formamide Wash Buffer was removed and replaced with Sample Prep Wash Buffer during MERSCOPE set up. One hundred microliters of RNase Inhibitor (New England BioLabs M0314L) was added to 250  $\mu$ L of Imaging Buffer Activator (PN 203000015), and this mixture was added via the cartridge activation port to a prethawed and mixed MERSCOPE Imaging cartridge (VIZGEN PN1040004). Fifteen milliliters of mineral oil (Millipore-Sigma m5904-6X500ML) were added to the activation port, and the MERSCOPE fluidics system was primed according to VIZGEN instructions. The flow chamber was assembled with the hybridized and cleared section coverslip according to VIZGEN specifications and the imaging session was initiated after collection of a 10X mosaic DAPI image and selection of the imaging area. For specimens that passed the minimum count threshold, imaging was initiated and processing was completed according to VIZGEN proprietary protocol.

The 140-gene human cortical panel was selected using a combination of manual and algorithmic based strategies requiring a reference single-cell RNA-seq or snRNA-seq dataset from the same tissue, in this case the human MTG snRNA-seq dataset and resulting taxonomy (17). First, an initial set of high-confidence marker genes are selected through a combination of literature search and analysis of the reference data. These genes are used as input for a greedy algorithm (detailed below). Second, the reference RNA-seq dataset is filtered to only include genes compatible with mFISH. Retained genes need to be (i) long enough to allow probe design ( $>960$  base pairs), (ii) expressed highly enough to be detected (FPKM  $\geq 10$ ) but not so high as to overcrowd the signal of other genes in a cell (FPKM  $<500$ ), (iii) expressed with low expression in off-target cells (FPKM  $<50$  in non-neuronal cells), and (iv) differentially expressed between cell types (top-500 remaining genes by marker score20). To more evenly sample each cell type, the reference dataset is also filtered to include a maximum of 50 cells per cluster.

The spatial distribution of human MTG cell types was estimated from several sections from two donors. For each section, we made two manual annotations: a parallelogram spanning pia to white matter that selected cells from all cortical layers and a line segment from pia to white matter along the local cortical column axis. The cortical depth was calculated as the projection of the coordinates of the selected cells onto the cortical column axis. Annotations were done in napari using a notebook:

[https://github.com/AllenInstitute/Great\\_Ape\\_MTG/blob/master/cell\\_type\\_mapping/Great\\_apes\\_subsetting\\_cortical\\_depth.ipynb](https://github.com/AllenInstitute/Great_Ape_MTG/blob/master/cell_type_mapping/Great_apes_subsetting_cortical_depth.ipynb).

#### Cell-type mapping in MERSCOPE data

Any genes not matched across both the MERSCOPE gene panel and the snRNA-seq mapping taxonomy were filtered from the snRNA-seq dataset. We calculated the mean gene expression for each gene in each snRNA-seq cluster. We assigned MERSCOPE cells to snRNA-seq clusters by finding the nearest cluster to the mean expression vectors of the snRNA-seq clusters using the cosine distance. All scripts and data used are available at [https://github.com/AllenInstitute/Great\\_Ape\\_MTG](https://github.com/AllenInstitute/Great_Ape_MTG).

The main step of gene selection uses a greedy algorithm to iteratively add genes to the initial set. To do this, each cell in the filtered reference dataset is mapped to a cell type by taking the Pearson correlation of its expression with each cluster median using the initial gene set of size  $n$ , and the cluster corresponding to the maximum value is defined as the “mapped cluster.” The “mapping distance” is then defined as the average cluster distance between the mapped cluster and the originally assigned cluster for each cell. In this case a weighted cluster distance, defined as one minus the Pearson correlation between cluster medians calculated across all filtered genes, is used to penalize cases where cells are mapped to very different types, but an unweighted distance, defined as the fraction of cells that do not map to their assigned cluster, could also be used. This mapping step is repeated for every possible  $n + 1$  gene set in the filtered reference dataset, and the set with minimum cluster distance is retained as the new gene set. These steps are repeated using the new get set (of size  $n + 1$ ) until a gene panel of the desired size is attained. Code for reproducing this gene selection strategy is available as part of the mfishtools R library (<https://github.com/AllenInstitute/mfishtools>).

We used our 140-gene MERFISH panel designed to identify human cortical cell types to map every type described in this updated human MTG taxonomy to determine cell-type locations within cortex and confirm cell-type proportions. All cell-type locations are provided for reference in graphical format as localized in a representative human MTG section H19.30.001.Cx46.MTG.02.02.007.5 (data S1).

#### RNAscope

Fresh-frozen human postmortem brain tissues were sectioned at 16 to 25  $\mu$ m onto Superfrost Plus glass slides (Fisher Scientific). Sections were dried for 20 min on dry ice and then vacuum sealed and stored at  $-80^{\circ}\text{C}$  until use. The RNAscope multiplex fluorescent V2 kit was used per the manufacturer’s instructions for

fresh-frozen tissue sections (ACD Bio), except that slides were fixed 60 min in 4% paraformaldehyde in IX PBS at  $4^{\circ}\text{C}$  and treated with protease for 15 min. Sections were imaged using a 40 $\times$  oil immersion lens on a Nikon TiE fluorescence microscope equipped with NIS-Elements Advanced Research imaging software (v4.20, RRID:SCR\_014329). Positive cells were called by manual assessment of RNA spots for each gene. Cells were called positive for a gene if they contained  $\geq 5$  RNA spots for that gene.

High versus low expression of *CUX2* was determined by measuring fluorescence intensity for that gene in ImageJ. Lipofuscin autofluorescence was distinguished from RNA spot signal based on the broad fluorescence spectrum and larger size of lipofuscin granules. Staining for each probe combination was repeated with similar results on at least two separate individuals and on at least two sections per individual. Images were assessed with the FIJI distribution of ImageJ v1.52p and with NIS-Elements v4.20. RNAscope probes used were *CUX2* (ACD Bio, 425581-C3), *LDB2* (1003951-C2), and *SMYD1* (493951-C2).

Fresh-frozen marmoset brain tissue was sectioned and processed for RNAscope staining as described above for human. Sections were imaged with a 10 $\times$  lens on a Nikon TiE fluorescence microscope to collect large overview images and smaller regions of tissue were re-imaged using a 40 $\times$  oil immersion lens. Images were assessed as above for human except that lipofuscin autofluorescence was not apparent in marmoset tissues. RNAscope probes used were *CUX2* (ACD Bio, 554631-C2), *NTNG2* (ACD Bio, custom probe targeting base pairs 1894 to 2819 of XM\_035261022.2), and *MGAT4C* (custom probe targeting base pairs 704 to 1799 of XM\_035257223.2). Staining for this probe combination was repeated on three sections from one individual. On all sections, an area of probe signal dropout was noted at the same location in the secondary auditory cortex that we attribute to a potential imaging or experimental artifact. All three probes had reduced signal intensity in this area, and the area is marked in the figure panel displaying the RNAscope data (Fig. 2F) with a red asterisk.

#### Analysis of great ape species pairwise comparison for glial cells

We used 10x snRNA-seq data for the comparison of normalized gene expression across species. Significant differential gene expression in pairwise comparisons of glial cells (astrocytes, microglia, oligodendrocytes) across great ape species was determined at log<sub>2</sub> fold-change  $>0.5$  and FDR  $<0.01$ . Among DEGs from great ape pairwise comparisons, species-specific highly divergent genes were identified as having  $>10$ -fold change in expression in a given species relative to the other two great ape species, and

with a threshold of gene expression of normalized gene counts >5 in at least one species. GO enrichment analysis was performed using the Bioconductor package “clusterProfiler” (<https://bioconductor.org/packages/release/bioc/html/clusterProfiler.html>), and the Fisher’s exact test was used for SynGO enrichment analysis (<https://www.syngoportal.org/>). GO and SynGO analyses were performed on the union of DEGs from the pairwise comparison between human and chimpanzee and the pairwise comparison between human and gorilla to increase power to detect significant GO terms. GO terms under biological process, molecular function, and cellular component categories were considered in the analysis. Significance for enriched terms was determined at 5% FDR. All MTG expressed genes in the consensus cell types (astrocytes, microglia, oligodendrocytes) were considered as the background gene set in the respective analyses. Gene expression change in glial cell types shown in heatmaps (Fig. 3E and figs. S5, A, B, and G, and S6, E and F) is calculated as the log<sub>2</sub> ratio of normalized expression counts in a given species relative to the other two great ape species. To analyze astrocyte genes associated with perisynaptic astrocytic processes, a list of genes encoding proteins enriched at astrocyte-neuron junctions was used from a proteomic study in the mouse cortex (29). To analyze microglia genes associated with intercellular communication and signaling, a list of genes predicted to act as the ligand-receptor interactome of microglia-neuron communication was used from a recent study in the mouse cortex (85).

#### Enrichment of HARs and hCONDELs near hDEGs

The set of HARs used in our analysis was obtained from (14), and the set of HAQERs used in our analysis was obtained from (47). The set of hCONDELs was obtained from (45, 46), and only hCONDELs that could be mapped to a syntenic orthologous location in hg38 were retained (1175 total) (86). We assigned intronic HARs, HAQERs, and hCONDELs to the genes they are intronic to and intergenic HARs, HAQERs, and hCONDELs to the closest upstream and downstream genes (table S8) using Ensembl GRCh38 annotations obtained in May 2021 and Ensembl Pan\_tro\_3.0, gorGor4, and Mmul\_10 annotations obtained in January 2023. With respect to the human annotations, 63.2% of HARs, 53.7% of HAQERs, and 59.4% of hCONDELs are intronic. For 83.2% of the 1165 intergenic HARs, at least one of their assigned genes is within 100 kb. For 90.7% of the 732 intergenic HAQERs, at least one of their assigned genes is within 100 kb. For 85.5% of the 477 intergenic hCONDELs, at least one of their assigned genes is within 100 kb. The proportion of intronic and intergenic HARs and hCONDELs is similar for the chimpanzee, gorilla, and macaque annotations. We consid-

ered HARs, HAQERs, and hCONDELs to be enriched near DEGs in a specific cell type if they are significant at 5% FDR for both of the following tests (87): (i) Are DEGs enriched for genes near HARs, HAQERs, and/or hCONDELs (Fisher’s exact test)? We set the background as expressed genes, which adjusts for the fact that HARs, HAQERs, and hCONDELs are known to be enriched near neural genes. (ii) Are HARs, HAQERs, and/or hCONDELs more likely to fall near DEGs than expected by chance? We assigned each gene a regulatory domain that comprises the genomic interval containing the gene along with the upstream and downstream intergenic regions that extend to the nearest flanking genes, with an upper bound of 5 Mb in total size. We then asked whether HARs, HAQERs, and hCONDELs are enriched within the regulatory domains of DEGs using the binomial test. This takes into account differences in genomic structure between genes, under the assumption that HARs, HAQERs, and hCONDELs will be more likely to fall within the regulatory domains of genes with large intronic or flanking regions by chance.

#### SynGO and synaptic gene family enrichment

To analyze the association between synaptic terms and human divergent gene expression patterns, we used an expert-curated database of GO annotations of synapse-related terms known as SynGO (28). To test whether hDEGs and hDEGs near HARs and hCONDELs are enriched in SynGO terms, we used Fisher’s exact test. We focused on SynGO terms within the first and second hierarchical levels of SynGO that broadly comprise the entire range of Cellular Components (CC) and Biological Processes (BP) terms, allowing for the visualization of enrichment patterns across a wide range of synaptic localizations and processes (fig. S18). We grouped SynGO terms into two levels based on their hierarchical organization in SynGO (<https://www.syngoportal.org/>), corresponding to the following reference codes: 11 terms within level 1 (A1, B1, C1, D1, E1, F1, G1, H1, I1, J1, K1) and 71 terms within level 2 (A2-3, B2-11, C2, D2-I1, E2, F2-10, G2-7, H2-4, I2-15, J2-11, K2-6). For synaptic gene families, we examined 15 functionally related categories: (i) families of cell-adhesion and synaptic-adhesion molecules, (ii) families of ligand-receptor complexes involved in growth factor signaling, (iii) families of other cell-surface receptors and ligands, (iv) families of other G protein-coupled receptors (GPCRs) and their ligands (including orphan GPCRs), (v) families of ligand-receptor complexes involved in neuropeptidergic signaling and related GPCRs and ligands, (vi) families of neurotransmitter-gated receptors and other ligand-gated receptors (including glutamate ionotropic receptors), (vii) Ras GTPase superfamily, (viii) families of Ras GAP and GEF signaling molecules, (ix) families of other regulatory

molecules and structural scaffolding proteins, (x) families related to other signaling complexes including intracellular kinases and phosphatases, (xi) families related to the ECM and proteoglycan families, (xii) families related to cytoskeletal composition and organization and other related proteins, (xiii) families involved in synaptic vesicle exocytosis and other membrane fusion components, (xiv) families of proteases and peptidases, and (xv) families of voltage-gated ion channels and other gated ion channels and solute transporters. For each of these, we assembled a comprehensive list based on HGNC reference and a previously curated catalog of synaptic molecules (88) (table S8). Significance was determined at 5% FDR. “All” genes are genes that are expressed and can be assessed for differential expression by DESeq2 in at least one consensus type.

#### REFERENCES AND NOTES

1. L. Papeo, B. Agostini, A. Lingnau, The large-scale organization of gestures and words in the middle temporal gyrus. *J. Neurosci.* **39**, 5966–5974 (2019). doi: [10.1523/JNEUROSCI.2668-18.2019](https://doi.org/10.1523/JNEUROSCI.2668-18.2019); pmid: [3126999](https://pubmed.ncbi.nlm.nih.gov/3126999)
2. A. Özyürek, Hearing and seeing meaning in speech and gesture: Insights from brain and behaviour. *Philos. Trans. R. Soc. London Ser. B* **369**, 20130296 (2014). doi: [10.1098/rstb.2013.0296](https://doi.org/10.1098/rstb.2013.0296); pmid: [25092664](https://pubmed.ncbi.nlm.nih.gov/25092664)
3. A. Kozenko et al., Evolution of regulatory signatures in primate cortical neurons at cell-type resolution. *Proc. Natl. Acad. Sci. U.S.A.* **117**, 28422–28432 (2020). doi: [10.1073/pnas.2011884117](https://doi.org/10.1073/pnas.2011884117); pmid: [33109720](https://pubmed.ncbi.nlm.nih.gov/33109720)
4. L. Roumazelles et al., Longitudinal connections and the organization of the temporal cortex in macaques, great apes, and humans. *PLOS Biol.* **18**, e3000810 (2020). doi: [10.1371/journal.pbio.3000810](https://doi.org/10.1371/journal.pbio.3000810); pmid: [32735557](https://pubmed.ncbi.nlm.nih.gov/32735557)
5. D. J. Ardesch et al., Evolutionary expansion of connectivity between multimodal association areas in the human brain compared with chimpanzees. *Proc. Natl. Acad. Sci. U.S.A.* **116**, 7101–7106 (2019). doi: [10.1073/pnas.1818521116](https://doi.org/10.1073/pnas.1818521116); pmid: [30886094](https://pubmed.ncbi.nlm.nih.gov/30886094)
6. E. Khrameev et al., Single-cell-resolution transcriptome map of human, chimpanzee, bonobo, and macaque brains. *Genome Res.* **30**, 776–789 (2020). doi: [10.1101/gr.256958.119](https://doi.org/10.1101/gr.256958.119); pmid: [32424074](https://pubmed.ncbi.nlm.nih.gov/32424074)
7. Z. He et al., Comprehensive transcriptome analysis of neocortical layers in humans, chimpanzees and macaques. *Nat. Neurosci.* **20**, 886–895 (2017). doi: [10.1038/nn.4548](https://doi.org/10.1038/nn.4548); pmid: [28414332](https://pubmed.ncbi.nlm.nih.gov/28414332)
8. S. Berto et al., Accelerated evolution of oligodendrocytes in the human brain. *Proc. Natl. Acad. Sci. U.S.A.* **116**, 24334–24342 (2019). doi: [10.1073/pnas.1907982116](https://doi.org/10.1073/pnas.1907982116); pmid: [31712436](https://pubmed.ncbi.nlm.nih.gov/31712436)
9. S. Ma et al., Molecular and cellular evolution of the primate dorsolateral prefrontal cortex. *Science* **377**, eab07257 (2022). doi: [10.1126/science.abb7257](https://doi.org/10.1126/science.abb7257); pmid: [36007006](https://pubmed.ncbi.nlm.nih.gov/36007006)
10. F. M. Krienen et al., Innovations present in the primate interneuron repertoire. *Nature* **586**, 262–269 (2020). doi: [10.1038/s41586-020-2781-z](https://doi.org/10.1038/s41586-020-2781-z); pmid: [32999462](https://pubmed.ncbi.nlm.nih.gov/32999462)
11. R. Fang et al., Conservation and divergence in cortical cellular organization between human and mouse revealed by single-cell transcriptome imaging. *bioRxiv* 2021.11.01.466826 [Preprint] (2021); <https://doi.org/10.1101/2021.11.01.466826>.
12. T. E. Bakken et al., Comparative cellular analysis of motor cortex in human, marmoset and mouse. *Nature* **598**, 111–119 (2021). doi: [10.1038/s41586-021-03465-8](https://doi.org/10.1038/s41586-021-03465-8); pmid: [34616062](https://pubmed.ncbi.nlm.nih.gov/34616062)
13. N. M. Foley et al., A genomic timescale for placental mammal evolution. *Science* **380**, eabl8189 (2023). doi: [10.1126/science.abl8189](https://doi.org/10.1126/science.abl8189); pmid: [37104581](https://pubmed.ncbi.nlm.nih.gov/37104581)
14. K. M. Girsik et al., Rewiring of human neurodevelopmental gene regulatory programs by human accelerated regions. *Neuron* **109**, 3239–3251.e7 (2021). doi: [10.1016/j.neuron.2021.08.005](https://doi.org/10.1016/j.neuron.2021.08.005); pmid: [34478631](https://pubmed.ncbi.nlm.nih.gov/34478631)
15. A. Nott et al., Brain cell type-specific enhancer-promoter interactome maps and disease-risk association. *Science* **366**, 1134–1139 (2019). doi: [10.1126/science.aay0793](https://doi.org/10.1126/science.aay0793); pmid: [31728786](https://pubmed.ncbi.nlm.nih.gov/31728786)

16. M. Song *et al.*, Cell-type-specific 3D epigenomes in the developing human cortex. *Nature* **587**, 644–649 (2020). doi: [10.1038/s41586-020-2825-4](https://doi.org/10.1038/s41586-020-2825-4); pmid: [33057195](https://pubmed.ncbi.nlm.nih.gov/33057195/)
17. R. D. Hodge *et al.*, Conserved cell types with divergent features in human versus mouse cortex. *Nature* **573**, 61–68 (2019). doi: [10.1038/s41586-019-1506-7](https://doi.org/10.1038/s41586-019-1506-7); pmid: [31435019](https://pubmed.ncbi.nlm.nih.gov/31435019/)
18. T. Stuart *et al.*, Comprehensive integration of single-cell data. *Cell* **177**, 1888–1902.e21 (2019). doi: [10.1016/j.cell.2019.05.031](https://doi.org/10.1016/j.cell.2019.05.031); pmid: [31178118](https://pubmed.ncbi.nlm.nih.gov/31178118/)
19. C. Hafemeister, R. Satija, Normalization and variance stabilization of single-cell RNA-seq data using regularized negative binomial regression. *Genome Biol.* **20**, 296 (2019). doi: [10.1186/s13059-019-1874-1](https://doi.org/10.1186/s13059-019-1874-1); pmid: [31870423](https://pubmed.ncbi.nlm.nih.gov/31870423/)
20. J. Berg *et al.*, Human neocortical expansion involves glutamatergic neuron diversification. *Nature* **598**, 151–158 (2021). doi: [10.1038/s41586-021-03813-8](https://doi.org/10.1038/s41586-021-03813-8); pmid: [34616067](https://pubmed.ncbi.nlm.nih.gov/34616067/)
21. N. L. Jorstad *et al.*, Transcriptomic cytoarchitecture reveals principles of human neocortex organization. *Science* **382**, eadf6812 (2023).
22. F. M. Krienen *et al.*, A marmoset brain cell census reveals regional specialization of cellular identities. *Sci. Adv.* **9**, eadk3986 (2023); doi: [10.1123/sciadv.adk3986](https://doi.org/10.1123/sciadv.adk3986).
23. G. Liu *et al.*, p130CAS is required for netrin signaling and commissural axon guidance. *J. Neurosci.* **27**, 957–968 (2007). doi: [10.1523/JNEUROSCI.4616-06.2007](https://doi.org/10.1523/JNEUROSCI.4616-06.2007); pmid: [17251438](https://pubmed.ncbi.nlm.nih.gov/17251438/)
24. R. Ayala *et al.*, Structure and regulation of the human INO80-nucleosome complex. *Nature* **556**, 391–395 (2018). doi: [10.1038/s41586-018-0021-6](https://doi.org/10.1038/s41586-018-0021-6); pmid: [29643506](https://pubmed.ncbi.nlm.nih.gov/29643506/)
25. A. Takano, R. Zochi, M. Hibi, T. Terashima, Y. Katsuyama, Function of strawberry notch family genes in the zebrafish brain development. *Kobe J. Med. Sci.* **56**, E220–E230 (2011). pmid: [21937870](https://pubmed.ncbi.nlm.nih.gov/21937870/)
26. K. Bulayeva *et al.*, Genomic structural variants are linked with intellectual disability. *J. Neural Transm.* **122**, 1289–1301 (2015). doi: [10.1007/s00702-015-1366-8](https://doi.org/10.1007/s00702-015-1366-8); pmid: [25626716](https://pubmed.ncbi.nlm.nih.gov/25626716/)
27. U. Braunschweig *et al.*, Widespread intron retention in mammals functionally tunes transcriptomes. *Genome Res.* **24**, 1774–1786 (2014). doi: [10.1101/gr.177790.114](https://doi.org/10.1101/gr.177790.114); pmid: [25258385](https://pubmed.ncbi.nlm.nih.gov/25258385/)
28. F. Koopmans *et al.*, SynGO: An evidence-based, expert-curated knowledge base for the synapse. *Neuron* **103**, 217–234.e4 (2019). doi: [10.1016/j.neuron.2019.05.002](https://doi.org/10.1016/j.neuron.2019.05.002); pmid: [31171447](https://pubmed.ncbi.nlm.nih.gov/31171447/)
29. T. Takano *et al.*, Chemico-genetic discovery of astrocytic control of inhibition in vivo. *Nature* **588**, 296–302 (2020). doi: [10.1038/s41586-020-2926-0](https://doi.org/10.1038/s41586-020-2926-0); pmid: [33177716](https://pubmed.ncbi.nlm.nih.gov/33177716/)
30. J. A. Stogsdill *et al.*, Astrocyte neuroglutins control astrocyte morphogenesis and synaptogenesis. *Nature* **551**, 192–197 (2017). doi: [10.1038/nature24638](https://doi.org/10.1038/nature24638); pmid: [29120426](https://pubmed.ncbi.nlm.nih.gov/29120426/)
31. T. R. Hammond, D. Robinton, B. Stevens, Microglia and the brain: Complementary partners in development and disease. *Annu. Rev. Cell Dev. Biol.* **34**, 523–544 (2018). doi: [10.1146/annurev-cellbio-100616-060509](https://doi.org/10.1146/annurev-cellbio-100616-060509); pmid: [30089221](https://pubmed.ncbi.nlm.nih.gov/30089221/)
32. M. S. Thion, F. Ginhoux, S. Garel, Microglia and early brain development: An intimate journey. *Science* **362**, 185–189 (2018). doi: [10.1126/science.aat0474](https://doi.org/10.1126/science.aat0474); pmid: [30309946](https://pubmed.ncbi.nlm.nih.gov/30309946/)
33. R. Fang *et al.*, Conservation and divergence of cortical cell organization in human and mouse revealed by MERFISH. *Science* **377**, 56–62 (2022). doi: [10.1126/science.abm1741](https://doi.org/10.1126/science.abm1741); pmid: [35771910](https://pubmed.ncbi.nlm.nih.gov/35771910/)
34. L. Fellner, K. A. Jellinger, G. K. Wenning, N. Stefanova, Glial dysfunction in the pathogenesis of  $\alpha$ -synucleinopathies: Emerging concepts. *Acta Neuropathol.* **121**, 675–693 (2011). doi: [10.1007/s00401-011-0833-z](https://doi.org/10.1007/s00401-011-0833-z); pmid: [21562886](https://pubmed.ncbi.nlm.nih.gov/21562886/)
35. J. Brettschneider, K. Del Tredici, V. M.-Y. Lee, J. Q. Trojanowski, Spreading of pathology in neurodegenerative diseases: A focus on human studies. *Nat. Rev. Neurosci.* **16**, 109–120 (2015). doi: [10.1038/nrn3887](https://doi.org/10.1038/nrn3887); pmid: [25588378](https://pubmed.ncbi.nlm.nih.gov/25588378/)
36. D. A. Kia *et al.*, Identification of candidate Parkinson disease genes by integrating genome-wide association study, expression, and epigenetic data sets. *JAMA Neurol.* **78**, 464–472 (2021). doi: [10.1001/jamaneurol.2020.5257](https://doi.org/10.1001/jamaneurol.2020.5257); pmid: [33523105](https://pubmed.ncbi.nlm.nih.gov/33523105/)
37. J. D. Paskus, B. E. Herring, K. W. Roche, Kalirin and Trio: RhoGEFs in synaptic transmission, plasticity, and complex brain disorders. *Trends Neurosci.* **43**, 505–518 (2020). doi: [10.1016/j.tins.2020.05.002](https://doi.org/10.1016/j.tins.2020.05.002); pmid: [32513570](https://pubmed.ncbi.nlm.nih.gov/32513570/)
38. M. Crow, A. Paul, S. Ballouz, Z. J. Huang, J. Gillis, Characterizing the replicability of cell types defined by single cell RNA-sequencing data using MetaNeighbor. *Nat. Commun.* **9**, 884 (2018). doi: [10.1038/s41467-018-03282-0](https://doi.org/10.1038/s41467-018-03282-0); pmid: [29491377](https://pubmed.ncbi.nlm.nih.gov/29491377/)
39. S. Fischer, M. Crow, B. D. Harris, J. Gillis, Scaling up reproducible research for single-cell transcriptomics using MetaNeighbor. *Nat. Protoc.* **16**, 4031–4067 (2021). doi: [10.1038/s41596-021-00575-5](https://doi.org/10.1038/s41596-021-00575-5); pmid: [34234317](https://pubmed.ncbi.nlm.nih.gov/34234317/)
40. M. Lotfollahi *et al.*, Mapping single-cell data to reference atlases by transfer learning. *Nat. Biotechnol.* **40**, 121–130 (2022). doi: [10.1038/s41587-021-01001-7](https://doi.org/10.1038/s41587-021-01001-7); pmid: [34462589](https://pubmed.ncbi.nlm.nih.gov/34462589/)
41. A. M. M. Sousa *et al.*, Molecular and cellular reorganization of neural circuits in the human lineage. *Science* **358**, 1027–1032 (2017). doi: [10.1126/science.aah3456](https://doi.org/10.1126/science.aah3456); pmid: [29170230](https://pubmed.ncbi.nlm.nih.gov/29170230/)
42. M. A. Raghani *et al.*, Species-specific distributions of tyrosine hydroxylase-immunoreactive neurons in the prefrontal cortex of anthropoid primates. *Neuroscience* **158**, 1551–1559 (2009). doi: [10.1016/j.neuroscience.2008.10.058](https://doi.org/10.1016/j.neuroscience.2008.10.058); pmid: [19041377](https://pubmed.ncbi.nlm.nih.gov/19041377/)
43. M. Büttner, J. Ostner, C. L. Müller, F. J. Theis, B. Schubert, scCODA is a Bayesian model for compositional single-cell data analysis. *Nat. Commun.* **12**, 6876 (2021). doi: [10.1038/s41467-021-27105-6](https://doi.org/10.1038/s41467-021-27105-6); pmid: [34824236](https://pubmed.ncbi.nlm.nih.gov/34824236/)
44. M. J. Menezes *et al.*, The extracellular matrix protein laminin  $\alpha$ 2 regulates the maturation and function of the blood-brain barrier. *J. Neurosci.* **34**, 15260–15280 (2014). doi: [10.1523/JNEUROSCI.3678-13.2014](https://doi.org/10.1523/JNEUROSCI.3678-13.2014); pmid: [25392494](https://pubmed.ncbi.nlm.nih.gov/25392494/)
45. C. Y. McLean *et al.*, Human-specific loss of regulatory DNA and the evolution of human-specific traits. *Nature* **471**, 216–219 (2011). doi: [10.1038/nature09774](https://doi.org/10.1038/nature09774); pmid: [21390129](https://pubmed.ncbi.nlm.nih.gov/21390129/)
46. Z. N. Kronenberg *et al.*, High-resolution comparative analysis of great ape genomes. *Science* **360**, eaar6343 (2018). doi: [10.1126/science.aar6343](https://doi.org/10.1126/science.aar6343); pmid: [29880660](https://pubmed.ncbi.nlm.nih.gov/29880660/)
47. R. J. Mangar *et al.*, Adaptive sequence divergence forged new neurodevelopmental enhancers in humans. *Cell* **185**, 4587–4603.e23 (2022). doi: [10.1016/j.cell.2022.10.016](https://doi.org/10.1016/j.cell.2022.10.016); pmid: [36423581](https://pubmed.ncbi.nlm.nih.gov/36423581/)
48. D. Kostka, A. K. Holloway, K. S. Pollard, Developmental loci harbor clusters of accelerated regions that evolved independently in ape lineages. *Mol. Biol. Evol.* **35**, 2034–2045 (2018). doi: [10.1093/molbev/msy109](https://doi.org/10.1093/molbev/msy109); pmid: [29897475](https://pubmed.ncbi.nlm.nih.gov/29897475/)
49. A. T. Lee *et al.*, Pyramidal neurons in prefrontal cortex receive subtype-specific forms of excitation and inhibition. *Neuron* **81**, 61–68 (2014). doi: [10.1016/j.neuron.2013.10.031](https://doi.org/10.1016/j.neuron.2013.10.031); pmid: [24361076](https://pubmed.ncbi.nlm.nih.gov/24361076/)
50. H. Takahashi, A. M. Craig, Protein tyrosine phosphatases PTP $\delta$ , PTP $\sigma$ , and LAR: Presynaptic hubs for synapse organization. *Trends Neurosci.* **36**, 522–534 (2013). doi: [10.1016/j.tins.2013.06.002](https://doi.org/10.1016/j.tins.2013.06.002); pmid: [23835198](https://pubmed.ncbi.nlm.nih.gov/23835198/)
51. T. M. Kranz *et al.*, De novo mutations from sporadic schizophrenia cases highlight important signaling genes in an independent sample. *Schizophr. Res.* **166**, 119–124 (2015). doi: [10.1016/j.schres.2015.05.042](https://doi.org/10.1016/j.schres.2015.05.042); pmid: [26091878](https://pubmed.ncbi.nlm.nih.gov/26091878/)
52. T. M. Kranz *et al.*, Phenotypically distinct subtypes of psychosis accompany novel or rare variants in four different signaling genes. *EBioMedicine* **6**, 206–214 (2016). doi: [10.1016/j.ebiom.2016.03.008](https://doi.org/10.1016/j.ebiom.2016.03.008); pmid: [27121562](https://pubmed.ncbi.nlm.nih.gov/27121562/)
53. A. Cressant *et al.*, Loss-of-function of PTP $\gamma$  and  $\zeta$ , observed in sporadic schizophrenia, causes brain region-specific deregulation of monoamine levels and altered behavior in mice. *Psychopharmacology* **234**, 575–587 (2017). doi: [10.1007/s00213-016-4490-8](https://doi.org/10.1007/s00213-016-4490-8); pmid: [28025742](https://pubmed.ncbi.nlm.nih.gov/28025742/)
54. P. R. Burton *et al.*, Genome-wide association study of 14,000 cases of seven common diseases and 3,000 shared controls. *Nature* **447**, 661–678 (2007). doi: [10.1038/nature05911](https://doi.org/10.1038/nature05911); pmid: [17554300](https://pubmed.ncbi.nlm.nih.gov/17554300/)
55. H. Peng *et al.*, Morphological diversity of single neurons in molecularly defined cell types. *Nature* **598**, 174–181 (2021). doi: [10.1038/s41586-021-03941-1](https://doi.org/10.1038/s41586-021-03941-1); pmid: [34616072](https://pubmed.ncbi.nlm.nih.gov/34616072/)
56. M. Somel, R. Rohlf, X. Liu, Transcriptomic insights into human brain evolution: Acceleration, neutrality, heterochrony. *Curr. Opin. Genet. Dev.* **29**, 110–119 (2014). doi: [10.1016/j.gde.2014.09.001](https://doi.org/10.1016/j.gde.2014.09.001); pmid: [25233113](https://pubmed.ncbi.nlm.nih.gov/25233113/)
57. M. B. Dalva *et al.*, EphB receptors interact with NMDA receptors and regulate excitatory synapse formation. *Cell* **103**, 945–956 (2000). doi: [10.1016/S0092-8674\(00\)00197-5](https://doi.org/10.1016/S0092-8674(00)00197-5); pmid: [11136979](https://pubmed.ncbi.nlm.nih.gov/11136979/)
58. S. S. Margolis *et al.*, EphB-mediated degradation of the RhoA GEF Ephexin5 relieves a developmental brake on excitatory synapse formation. *Cell* **143**, 442–455 (2010). doi: [10.1016/j.cell.2010.09.038](https://doi.org/10.1016/j.cell.2010.09.038); pmid: [21029865](https://pubmed.ncbi.nlm.nih.gov/21029865/)
59. N.-P. Tsai *et al.*, Multiple autism-linked genes mediate synapse elimination via proteasomal degradation of a synaptic scaffold PSD-95. *Cell* **151**, 1581–1594 (2012). doi: [10.1016/j.cell.2012.11.040](https://doi.org/10.1016/j.cell.2012.11.040); pmid: [23260144](https://pubmed.ncbi.nlm.nih.gov/23260144/)
60. A. Q. Nguyen *et al.*, Astrocytic Ephrin-B1 controls excitatory-inhibitory balance in developing hippocampus. *J. Neurosci.* **40**, 6854–6871 (2020). doi: [10.1523/JNEUROSCI.0413-20.2020](https://doi.org/10.1523/JNEUROSCI.0413-20.2020); pmid: [32801566](https://pubmed.ncbi.nlm.nih.gov/32801566/)
61. G. N. Elston, R. Benavides-Piccione, J. DeFelipe, The pyramidal cell in cognition: A comparative study in human and monkey. *J. Neurosci.* **21**, RC163 (2001). doi: [10.1523/JNEUROSCI.21-17-00022001](https://doi.org/10.1523/JNEUROSCI.21-17-00022001); pmid: [11511694](https://pubmed.ncbi.nlm.nih.gov/11511694/)
62. J. F. Oliveira, V. M. Sardinha, S. Guerra-Gomes, A. Araque, N. Sousa, Do stars govern our actions? Astrocyte involvement in rodent behavior. *Trends Neurosci.* **38**, 535–549 (2015). doi: [10.1016/j.tins.2015.07.006](https://doi.org/10.1016/j.tins.2015.07.006); pmid: [26316036](https://pubmed.ncbi.nlm.nih.gov/26316036/)
63. E. Favuzzi *et al.*, GABAergic microglia selectively sculpt developing inhibitory circuits. *Cell* **184**, 4048–4063.e32 (2021). doi: [10.1016/j.cell.2021.06.018](https://doi.org/10.1016/j.cell.2021.06.018); pmid: [34233165](https://pubmed.ncbi.nlm.nih.gov/34233165/)
64. K. E. Poskanzer, R. Yuste, Astrocytes regulate cortical state switching in vivo. *Proc. Natl. Acad. Sci. U.S.A.* **113**, E2675–E2684 (2016). doi: [10.1073/pnas.1520791113](https://doi.org/10.1073/pnas.1520791113); pmid: [27122314](https://pubmed.ncbi.nlm.nih.gov/27122314/)
65. S. Mederos *et al.*, GABAergic signaling to astrocytes in the prefrontal cortex sustains goal-directed behaviors. *Nat. Neurosci.* **24**, 82–92 (2021). doi: [10.1038/s41593-020-00752-x](https://doi.org/10.1038/s41593-020-00752-x); pmid: [33288910](https://pubmed.ncbi.nlm.nih.gov/33288910/)
66. J. Nagai *et al.*, Behaviorally consequential astrocytic regulation of neural circuits. *Neuron* **109**, 576–596 (2021). doi: [10.1016/j.neuron.2020.12.008](https://doi.org/10.1016/j.neuron.2020.12.008); pmid: [33385325](https://pubmed.ncbi.nlm.nih.gov/33385325/)
67. P. Kofuji, A. Araque, Astrocytes and behavior. *Annu. Rev. Neurosci.* **44**, 49–67 (2021). doi: [10.1146/annurev-neuro-101920-112225](https://doi.org/10.1146/annurev-neuro-101920-112225); pmid: [33406370](https://pubmed.ncbi.nlm.nih.gov/33406370/)
68. A. Sharif *et al.*, Differential erbB signaling in astrocytes from the cerebral cortex and the hypothalamus of the human brain. *Glia* **57**, 362–379 (2009). doi: [10.1002/glia.20762](https://doi.org/10.1002/glia.20762); pmid: [18803307](https://pubmed.ncbi.nlm.nih.gov/18803307/)
69. S. P. Sardi, J. Murtie, S. Koirala, B. A. Patten, G. Corfas, Presenilin-dependent ErbB4 nuclear signaling regulates the timing of astrogenesis in the developing brain. *Cell* **127**, 185–197 (2006). doi: [10.1016/j.cell.2006.07.037](https://doi.org/10.1016/j.cell.2006.07.037); pmid: [17018285](https://pubmed.ncbi.nlm.nih.gov/17018285/)
70. U. S. Sandau *et al.*, The synaptic cell adhesion molecule, SynCAM1, mediates astrocyte-to-astrocyte and astrocyte-to-GnRH neuron adhesiveness in the mouse hypothalamus. *Endocrinology* **152**, 2353–2363 (2011). doi: [10.1210/en.2010-1434](https://doi.org/10.1210/en.2010-1434); pmid: [21486931](https://pubmed.ncbi.nlm.nih.gov/21486931/)
71. C. C. Sherwood *et al.*, Invariant synapse density and neuronal connectivity scaling in primate neocortical evolution. *Cereb. Cortex* **30**, 5604–5615 (2020). doi: [10.1093/cercor/cbaa149](https://doi.org/10.1093/cercor/cbaa149); pmid: [32488266](https://pubmed.ncbi.nlm.nih.gov/32488266/)
72. S. B. Carroll, Evo-devo and an expanding evolutionary synthesis: A genetic theory of morphological evolution. *Cell* **134**, 25–36 (2008). doi: [10.1016/j.cell.2008.06.030](https://doi.org/10.1016/j.cell.2008.06.030); pmid: [18614008](https://pubmed.ncbi.nlm.nih.gov/18614008/)
73. F. C. Jones *et al.*, The genomic basis of adaptive evolution in threespine sticklebacks. *Nature* **484**, 55–61 (2013). doi: [10.1038/nature10944](https://doi.org/10.1038/nature10944); pmid: [22481358](https://pubmed.ncbi.nlm.nih.gov/22481358/)
74. D. H. Geschwind, P. Rakic, Cortical evolution: Judge the brain by its cover. *Neuron* **80**, 633–647 (2013). doi: [10.1016/j.neuron.2013.10.045](https://doi.org/10.1016/j.neuron.2013.10.045); pmid: [24183016](https://pubmed.ncbi.nlm.nih.gov/24183016/)
75. N. A. Oberheim, S. A. Goldman, M. Nedergaard, Heterogeneity of astrocytic form and function. *Methods Mol. Biol.* **814**, 23–45 (2012). doi: [10.1007/978-1-61779-452-0\\_3](https://doi.org/10.1007/978-1-61779-452-0_3); pmid: [22144298](https://pubmed.ncbi.nlm.nih.gov/22144298/)
76. L. Geirsdottir *et al.*, Cross-species single-cell analysis reveals divergence of the primate microglia program. *Cell* **179**, 1609–1622.e16 (2019). doi: [10.1016/j.cell.2019.11.010](https://doi.org/10.1016/j.cell.2019.11.010); pmid: [31835035](https://pubmed.ncbi.nlm.nih.gov/31835035/)
77. C. X. Tan, C. Ergoju, Cell adhesion molecules regulating astrocyte-neuron interactions. *Curr. Opin. Neurobiol.* **69**, 170–177 (2021). doi: [10.1016/j.conb.2021.03.015](https://doi.org/10.1016/j.conb.2021.03.015); pmid: [33957433](https://pubmed.ncbi.nlm.nih.gov/33957433/)
78. A. Saunders *et al.*, Molecular diversity and specializations among the cells of the adult mouse brain. *Cell* **174**, 1015–1030.e16 (2018). doi: [10.1016/j.cell.2018.07.028](https://doi.org/10.1016/j.cell.2018.07.028); pmid: [30096299](https://pubmed.ncbi.nlm.nih.gov/30096299/)
79. G. Paxinos, C. Watson, M. Petrides, M. Rosa, H. Tokuno, *The Marmoset Brain in Stereotaxic Coordinates* (Elsevier, 2011).
80. R. L. Buckner, D. S. Margulies, Macroscale cortical organization and a default-like apex transmodal network in the marmoset monkey. *Nat. Commun.* **10**, 1976 (2019). doi: [10.1038/s41467-019-09812-8](https://doi.org/10.1038/s41467-019-09812-8); pmid: [31036823](https://pubmed.ncbi.nlm.nih.gov/31036823/)
81. R. L. Buckner, F. M. Krienen, The evolution of distributed association networks in the human brain. *Trends Cogn. Sci.* **17**, 648–665 (2013). doi: [10.1016/j.tics.2013.09.017](https://doi.org/10.1016/j.tics.2013.09.017); pmid: [24210963](https://pubmed.ncbi.nlm.nih.gov/24210963/)
82. C. S. McGinnis, L. M. Murrow, Z. J. Gartner, DoubletFinder: Doublet detection in single-cell RNA sequencing data using artificial nearest neighbors. *Cell Syst.* **8**, 329–337.e4 (2019). doi: [10.1016/j.cels.2019.03.003](https://doi.org/10.1016/j.cels.2019.03.003); pmid: [30954475](https://pubmed.ncbi.nlm.nih.gov/30954475/)
83. H. Suresh *et al.*, Comparative single-cell transcriptomic analysis of primate brains highlights human-specific regulatory evolution. *Nat. Ecol. Evol.* (2023). doi: [10.1038/s41559-023-02186-7](https://doi.org/10.1038/s41559-023-02186-7); pmid: [37667001](https://pubmed.ncbi.nlm.nih.gov/37667001/)
84. C. De Donno *et al.*, Population-level integration of single-cell datasets enables multi-scale analysis across samples.

bioRxiv 2022.11.28.517803 [Preprint] (2022); <https://doi.org/10.1101/2022.11.28.517803>.

85. J. A. Stogsdill *et al.*, Pyramidal neuron subtype diversity governs microglia states in the neocortex. *Nature* **608**, 750–756 (2022). doi: [10.1038/s41586-022-05056-7](https://doi.org/10.1038/s41586-022-05056-7); pmid: [35948630](#)
86. Y. Turakhia, H. I. Chen, A. Marcovitz, G. Bejerano, A fully-automated method discovers loss of mouse-lethal and human-monogenic disease genes in 58 mammals. *Nucleic Acids Res.* **48**, e91–e91 (2020). doi: [10.1093/nar/gkaa550](https://doi.org/10.1093/nar/gkaa550); pmid: [32614390](#)
87. C. Y. McLean *et al.*, GREAT improves functional interpretation of cis-regulatory regions. *Nat. Biotechnol.* **28**, 495–501 (2010). doi: [10.1038/nbt.1630](https://doi.org/10.1038/nbt.1630); pmid: [20436461](#)
88. C. Földy *et al.*, Single-cell RNAseq reveals cell adhesion molecule profiles in electrophysiologically defined neurons. *Proc. Natl. Acad. Sci. U.S.A.* **113**, E5222–E5231 (2016). doi: [10.1073/pnas.1610155113](https://doi.org/10.1073/pnas.1610155113); pmid: [27531958](#)

#### ACKNOWLEDGMENTS

We thank the tissue procurement, tissue processing, and facilities teams at the Allen Institute for Brain Science for assistance with the transport and processing of postmortem and neurosurgical brain specimens; the technology team at the Allen Institute for assistance with data management; C. Sobieski for assistance with RNAscope data generation; and M. Vawter, J. Davis, and the San Diego medical examiner's office for assistance with postmortem tissue donations. We thank M. Hawrylycz for improvements to taxonomy visualizations. This publication was supported by and coordinated through the NIH's Brain Research through Advancing Innovative Neurotechnologies (BRAIN) Initiative – Cell Census Network (BICCN). This publication is part of the Human Cell Atlas ([www.humancellatlas.org/publications/](http://www.humancellatlas.org/publications/)). Research reported in this publication was supported by the National Institute of Mental Health of the NIH under award nos. U01MH114812 and

U19MH114830. The content is solely the responsibility of the authors and does not necessarily represent the official views of the NIH. The authors thank the founder of the Allen Institute, Paul G. Allen, for his vision, encouragement, and support. **Funding:** This work was funded by the Allen Discovery Center for Human Brain Evolution (C.A.W., D.E.-A., J.H.T.S., M.B.); Dutch Research Council (NWO) Applied and Engineering Sciences (AES) grant 3DOMICS 17126 (B.P.L., J.E., T.H., T.K.); NWO Gravitation Program BRAINSCAPES 024.004.012 (B.P.L., S.B., T.H.); an EMBO Postdoctoral Fellowship (ALTF 336-2022) (D.E.A.); a Helen Hay Whitney Fellowship (J.H.T.S.); a Nancy and Buster Alvord Endowment (C.D.K.); a NARSAD Young Investigator Award (M.C.); NIH grants F32MH114501 (M.C.), HG011641 (C.C.S., W.D.H.), NS092988 (C.C.S., W.D.H.), R01 HG009318 (A.D.), R01LM012736 (H.S., J.Gi.), R01MH113005 (H.S., J.Gi.), U01MH114812 (A.M.Y., A.T., C.R., D.B., D.M., E.S.L., J.Go., K.Si., K.Sm., K.K., M.T., N.L.J., R.D.H., S.-L.D., S.L., T.E.B., T.P.), U01MH114819 (F.M.K., G.F., S.A.M.), U19MH114821 (H.S., J.Gi.), and U19MH114830 (A.G., A.T., D.B., D.M., J.Go., K.Sm., K.K., M.T., T.P.); NSF grant EF-2021785 (C.C.S., W.D.H.); and an Y. Eva Tan Postdoctoral Fellowship (J.H.S.). **Author contributions:** Sample preparation and RNA data generation: A.G., A.M.Y., A.T., C.C.S., C.D.K., C.R., D.B., D.M., E.S.L., F.M.K., G.F., J.Go., K.Si., K.Sm., K.K., M.T., R.D.H., S.A.M., S.-L.D., S.L., T.E.B., T.P., W.D.H.; Spatial transcriptomic data generation: B.L., D.M., E.G., J.C., S.C.S.; Data archive and infrastructure: J.Go., S.S.; Cytosplore Viewer software: B.P.L., J.E., S.B., T.H., T.K.; Data analysis: A.D., B.L., B.P.L., C.A.W., D.E.-A., E.G., E.S.L., F.M.K., H.S., J.C., J.E., J.Go., J.Gi., J.H.T.S., K.J.T., K.Sm., M.B., M.C., N.C.-P., N.L.J., S.B., S.C.S., T.E.B., T.H.; Data interpretation: A.D., C.A.W., C.C.S., D.E.-A., E.S.L., F.M.K., H.S., J.C., J.Go., J.Gi., J.H.T.S., K.J.T., M.B., M.C., N.C.-P., N.L.J., R.D.H., S.C.S., S.-L.D., T.E.B.; Writing manuscript: C.A.W., C.C.S., D.E.-A., E.S.L., J.C., J.Gi., J.H.T.S., N.L.J., R.D.H., T.E.B. **Competing interests:** N.L.J. has been an employee of Genentech since 11 April 2022. The other authors declare no competing interests. **Data and**

**materials availability:** Raw sequence data were produced as part of the BICCN (RRID:SCR\_015820) and are available for download from the Neuroscience Multi-omics Archive (RRID: SCR\_016152; <https://assets.nemoarchive.org/dat-net1412>) and the Brain Cell Data Center (RRID:SCR\_017266; <https://biccn.org/data>). Code for the analysis and generation of figures is available for download from [https://github.com/AllenInstitute/Great\\_Ape\\_MTG](https://github.com/AllenInstitute/Great_Ape_MTG). Visualization and analysis tools for integrated species comparison are available using Cytosplore Viewer (RRID:SCR\_018330; <https://viewer.cytosplore.org/>). These tools allow the comparison of gene expression in consensus clusters across species, as well as species-specific clusters, and the calculation of differential expression within and among species. The following publicly available datasets were used for analysis: Synaptic Gene Ontology (SynGO) and orthologous genes across species from NCBI Homologene (downloaded November 2019). MTG human SMARTSeq v4 data are available at <https://portal.brain-map.org/atlas-and-data/rnaseq/human-mtg-smart-seq> and <https://assets.nemoarchive.org/dat-swzf4kc>.

**License information:** Copyright © 2023 the authors, some rights reserved; exclusive licensee American Association for the Advancement of Science. No claim to original US government works. <https://www.science.org/about/science-licenses-journal-article-reuse>

#### SUPPLEMENTARY MATERIALS

[science.org/doi/10.1126/science.adc9516](https://science.org/doi/10.1126/science.adc9516)

Figs. S1 to S23

Tables S1 to S8

References

MDAR Reproducibility Checklist

Data S1

Submitted 19 September 2022; accepted 13 September 2023  
10.1126/science.adc9516